UCLA
UCLA Electronic Theses and Dissertations

Title

Monsoon onset and precipitation control by mid-latitude waves in modern and glacial climates

Permalink

Author

Lee, Hung-I

Publication Date

2019

Peer reviewed|Thesis/dissertation

UNIVERSITY OF CALIFORNIA

Los Angeles

Monsoon onset and precipitation control

by mid-latitude waves

in modern and glacial climates

A dissertation submitted in partial satisfaction

of the requirements for the degree

Doctor of Philosophy in Atmospheric and Oceanic sciences

by

Hung-I Lee

2019

ABSTRACT OF THE DISSERTATION

Monsoon onset and precipitation control

by mid-latitude waves

in modern and glacial climates

by

Hung-I Lee

Doctor of Philosophy in Atmospheric and Oceanic sciences

University of California, Los Angeles, 2019

Professor Aradhna K Tripati, Chair

We study North American summer monsoon (NASM) and East Asian summer monsoon (EASM) precipitation in modern and glacial climates from the perspective of mid-latitude wave dynamics. The thesis consists of two major parts: the study of summertime North America precipitation change since Last Glacial Maximum (LGM, 21ka), and dynamics of NASM/EASM precipitation in a modern climate. We begin our study by analyzing precipitation data from pollen reconstructed proxies and ERA-Interim reanalysis. We provide physical explanations using models with different levels of complexities including Paleoclimate Model Intercomparson Project (PMIP3), Laboratoire de Météorologie Dynamique (LMDZ), a simplified GCM [1], and semi-analytical models (the Charney-Eliassen model [2], the Eady model [3] and the two-layer quasi-geostrophic model [4]).

We first study the precipitation dipole, defined as moistening the American Southwest and drying the American Southeast during LGM, which has been identified through paleoproxy reconstructions and tested with climate model simulations. By analyzing the PMIP3 simulations, we suggest that the summertime stationary waves with NW-SE tilting and eastward phase-shifting in LGM enhance precipitation in the American southwest and also dry the American southeast. Numerical experiments performed with the LMDZ model indicate that Laurentide ice topography induces NW-SE tilting and an ice thermodynamic effect trig-

gers eastward phase-shifting of stationary waves. A new solution of the Charney-Eliassen model is derived to quantify that the phase-shifting correlates positively with the strengths of jet streams. By comparing a synthesis of LGM pollen proxies to the PMIP3 ensemble, we find models that simulate a weaker Laurentide ice thermodynamic effect, weaker stationary waves with greater NW-SE tilting, weaker phase-shifting, and weaker jet stream anomalies compare more favorably to the proxies. Since the thermal wind equation links meridional temperature gradients to vertical wind shear, the weaker summer polar amplification compares more favorably to the proxy.

Secondly, we use a global space-time diagram of column water vapor (CWV) at 30°N latitude from daily reanalysis data, and find two quasi-stationary parts of atmospheric rivers (QSARs) that feature locally enhanced CWV and evolve from the Eastern Pacific/Atlantic basins in the winter to the Western Pacific/Atlantic in the summer. East Asian Summer Monsoon (EASM) onset coincides with the time CWV in the Pacific QSAR first exceeds 40 mm, which also typically occurs just before it makes landfall. QSARs exist in 39-year (1979-2017) daily climatological CWV, demonstrating the seasonal cycles of these features are quasi-stationary and potentially useful for monsoon onset prediction. EASM onset is particularly predictable following El Niño Southern Oscillation (ENSO), consistently occurring 25-40 days after the QSAR crosses the dateline.

Given the fact that atmospheric rivers are lead by mid-latitude synoptic waves generated by baroclinic instability, we then study the dynamics of QSARs using theories of baroclinic instabilities. Simplified GCM experiments are applied to identify that the zonal anomalies of jet streams induced by the tropical warm pools-cold tongues trigger the formations of the QSAR-like features. Analysis of local wave activity (LWA) reveals QSARs as fronts of wave breakings, and indicates that QSARs are likely to be quasi-stationary baroclinic waves. These quasi-stationary baroclinic waves could be predicted semi-analytically by applying the Eady and the two-layer quasi-geostrophic models, thus opening a new window into dynamics of subtropical monsoon extensions.

The dissertation of Hung-I Lee is approved.

David K. Jacobs

Gang Chen

Jonathan Lloyd Mitchell

Aradhna K Tripati, Committee Chair

University of California, Los Angeles

2019

I dedicate this to my parents,

for their unresearved and eternal love.

TABLE OF CONTENTS

x

ACKNOWLEDGMENTS

work, and I attribute all my accomplishments to you.

2010	Bachelor of Science, Department of Physics (minor in Mathematics), National Taiwan University, R.O.C.
2016	Master of Science, Department of Atmospheric and Oceanic Sciences, University of California, Los Angeles, California, U.S.
2017	Candidate in Philosophy, Department of Atmospheric and Oceanic Sciences, University of California, Los Angeles, California, U.S.
2015–2018	Teaching Assistant, Department of Physics, and Department of Atmospheric and Oceanic Sciences, University of California, Los Angeles, California, U.S.
2018	Teaching Associate, Department of Atmospheric and Oceanic Sciences, University of California, Los Angeles, California, U.S.

PUBLICATIONS

Lee, H-I., Mitchell, J. L., Tripati, A.,Lora,J.M.,Chen,G., and Ding,Q.(2019). North Atlantic and Pacificquasi-stationary parts of atmosphericrivers and their implications for EastAsian monsoon onset. *Geophysical Research Letters,46.* https://doi.org/10.1029/2019GL084272

Lee, H-I., Mitchell, J. L., Tripati, A., and Lora,J.M. (*In Preparation*) The response of North American precipitation and temperature during LGM due to stationary waves in PMIP3 simulations.

CHAPTER 1

Introduction

Monsoons have conventionally been regarded as a seasonal alternating humid/dry period during summer/winter seasons, and usually occur in global subtropical areas. In the IPCC report, monsoon regions are defined when averaged daily precipitation during boreal summer (MJJAS) is 2.5 mm/day greater than during remaining seasons [5, 6]. According to the criterion, global monsoon regions occur in East/South Asia, North/South America, North/South Africa, and Australia, and more than half of human populations living in those regions rely on the water supply by monsoon systems. Hence, the responses of monsoon precipitation to future climate change gradually draw considerable attention. One way to study responses to future global warming scenarios of monsoons is to analyze data from Coupled Model Intercomparison Project 5 (CMIP5) simulations running under Representative Concentration Pathway 8.5 (RCP8.5, corresponding to the enhanced radiative forcing due to anthropogenic CO2 emissions). Analysis of CMIP5 model data indicates effects of future climate change on monsoon precipitation amounts, distributions and onsets. However, significant model disagreements among CMIP5 models indicate that our knowledge of monsoons is insufficient [5]. Therefore, to improve the climate model simulations, we focus on the study of monsoon theories and test climate model simulations against paleo-precipitation proxies.

Monsoons have long been conceived as seasonal alternating circulations of a local, large scale sea-breeze driven by land-sea contrasts in surface heating [7, 8]. Now, the general consensus is that monsoons are seasonal migrations of the Intertropical Convergence Zone (ITCZ). However, zonal asymmetries of the ITCZ in the East Asian and North American monsoon sectors, which feature the local extensions of rain-belts into mid-latitudes, indicate that this zonally symmetric perspective is incomplete. Hence, to study monsoon theories, we

rely on data analysis provided by ERA-Interim Reanalysis [9] for modern climates and pollen reconstructed precipitation proxies for glacial periods [10]. In this chapter, we summarize several paleoclimate studies of North America during LGM and monsoon theory from the perspective of dynamics and thermodynamics. We also briefly introduce mid-latitude wave dynamics that will be applied for developing a monsoon theory.

1.1   Dynamics of monsoon circulations

In the traditional view, monsoon circulations are thermally driven by different heat capacities of the land and ocean. However, this view fails to explain the occurrence of coastal desert such as in Arabian Peninsula and in North Africa. Nowadays, monsoon circulations are widely thought of as seasonal migrations of the ITCZ in the upward branch Hadley circulations. Therefore, studying monsoon dynamics is equivalent to understanding onset of regime transitions in Hadley (overturning) circulations [11, 12].

Given the complexity of Hadley circulations, existing theories of them are split into several hierarchies, depending on different controlling factors. An example of a theory that applies to the zonally averaged Hadley circulations ([13], HH80 hereafter) assumes nonlinear inviscid and dry fluids on a rotating frame with simplified, constant heating. Under the previous assumptions, meridional transports by thermally driven Hadley circulations follow angular momentum conservation. The cell width is then determined by conservation of energy and continuity of potential temperature.

A seasonal migration of solar heating pattern is later added into the HH80 model to generate hemispherically asymmetric Hadley circulations [14, 15]. Emanuel [16] further extended the HH80 to include moisture using a fixed vertical moist adiabatic lapse rate. These early works suppressed the effects of the baroclinic eddies on Hadley circulations. Although the approximation is unrealistic, axisymmetric models of have provided invaluable insight into Hadley cell dynamics. The next step to study dynamics of the Hadley circulations is to consider its relation to nonlinear baroclinic eddies. A simple approximation that horizontal eddy momentum flux divergence fed by baroclinic instability dominates over vertical flux

convergence is made based on the fact that the vertical scale height of the atmosphere is relatively smaller than horizontal length scales. Hence, for a zonally averaged fluid with only horizontal eddy transport in a rotating frame, the steady-state vorticity equation can be written as,

$$(f + \overline{\zeta})\overline{v} = \frac{1}{a \cos^2 \phi} \frac{\partial}{\partial \phi}(\cos^2 \phi \overline{u'v'}) - r\overline{\zeta}^4 \tag{1.1}$$

where $f + \overline{\zeta}$ is absolute vorticity, f is the Coriolis parameter, ζ is relative vorticity, ϕ is latitude, u is zonal wind, v is meridional wind and r is surface friction. A bar denotes zonal average, and a prime denotes zonal asymmetries. The absolute vorticity is also propotional to meridional gradients of angular momentum,

$$(f + \overline{\zeta}) = -\frac{1}{a^2 \cos \phi} \frac{\partial \overline{m}}{\partial \phi} \tag{1.2}$$

and

$$\overline{m} = (\overline{u} + \Omega a \cos \phi) a \cos \phi \tag{1.3}$$

where m is angular momentum, Ω is angular velocity of the Earth. In non-linear inviscid fluid, an absolute vorticity term remains, and Eq. 1.1 collapses into $(f + \overline{\zeta})\overline{v} = 0$. Therefore, nonzero meridional motion $\overline{v}$ only exists in the angular-momentum-conserving regime, that is $f + \overline{\zeta} = 0$ (obtained by Eq. 1.2).

The lack of nonlinear mathematical tools to solve the vorticity equation hinders scientists to approach an analytical solution of the Hadley circulations influenced by baroclinic eddies. Aqua-planet numerical simulations [17, 12] are applied to realize the effects of baroclinic eddies on Hadley circulations rather than searching for complete analytic solutions. In [12], a local Rossby number ($Ro = -\overline{\zeta}/f$) was defined to trace local effects of eddies on Hadley circulations. If $Ro \to 1$, then the solution is close to HH80, and when $Ro \to 0$ eddy momentum flux divergences play a dominant role in the vorticity equation. Areas of significant eddy influence are in the downward branch of Hadley circulation where baroclinic eddies break and mix.

3

Although it is proven that baroclinic eddies have a strong influence in the downward branch of the Hadley circulation over winter mid-latitude [12], the complete physical story of how baroclinic eddies complete downward branches of Hadley circulations still needs explanation. Based on the paradigm of geostrophic turbulence, coherent eddy structures (Rossby wave and breaking Rossby waves in this event) are generated before losing predictabilities. Therefore, understanding how Rossby waves complete Hadley circulations becomes a current issue in studying monsoon theory [18, 19]. [18] used a moist general circulation model (GCM) and observed that Rossby waves trigger monsoon onsets from the Hovmöller plot of precipitation. However, [19] applied a similar method but found that Rossby waves actually hinder monsoon onset. Hence, understanding of baroclinic eddies on monsoon onset still remains a challenging question.

An advanced approach to hierarchy monsoon theory is to study topographic effects on Hadley circulations. One famous example is how topographic vertical gravity waves cause the formation of the deserts in East Africa [20]. Another simulation work highlights the strengthening of EASM by adding Himalayan mountain ridges [21], and in particular how the vertical moist lapse rate is modified by Himalayan mountain ridges contributes to the enhanced monsoon precipitation in East Aisa.

1.2 Thermodynamics of monsoon circulations

In the previous section, theories of inviscid and steady flow without baroclinic eddies in a dry, zonally symmetric climate show that monsoon overturning circulations onset when absolute vorticity reaches zero ($(f + \overline{\zeta})\overline{v} = 0$) and this fact indicates that f and $\overline{\zeta}$ have opposite signs ($f = -\overline{\zeta}$). Hence, the criterion of monsoon onset could be defined as

$$f\overline{\zeta} < 0 \tag{1.4}$$

A key argument of the monsoon theories is that the flow would relax toward the radiative equilibrium quickly (by Newtonian cooling in this case [15]). The relaxation via this diabatic heating is even faster than the heat exchange via monsoon overturning circulations.

4

Therefore, we could assume that the air temperature is close to the temperature at radiative equilibrium (T_e). Using thermal wind balance, the zonal wind ($\overline{u}$) could be obtained with the knowledge of Te given by HH80 by assuming zero surface winds. Plugging the radiative equilibrium solution of the vertically integrated $\overline{u}$ into relative vorticity ($\overline{\zeta} = \frac{\partial \overline{u}}{\partial y}$), Eq. 1.4 could be rewritten as

$$-\frac{gD}{T_0}\frac{\sin\phi}{\cos^3\phi}\frac{\partial}{\partial\phi}\left(\frac{\cos^3\phi}{\sin\phi}\frac{\partial \hat{T}_e}{\partial\phi}\right) < f^2 a^2 \tag{1.5}$$

where g is gravitational acceleration, D is the height of troposphere, T_0 is the global averaged temperature, and hat denotes vertical integration throughout the troposphere so that $\hat{T}_e = \frac{1}{D}\int_0^D T_e dz$ (see derivations in [15]).

Eq. 1.5 could be further extended to a moist atmosphere [16] by assuming that the air flow follows moist adiabatic equilibrium. The approximation is made based on the argument that air flows also reach convective equilibrium faster than monsoon overturning circulations. Hence, this approximation is also called convective quasi-equilibrium (CQE) and has been tested in a simplified moist GCM [22]. CQE allows us to rewrite Eq. 1.5 with only the knowledge of near surface (planetary boundary layer) equivalent potential temperature (see derivations in [16])

$$-\frac{\sin\phi}{\cos^3\phi}\frac{\partial}{\partial\phi}\left(\frac{\cos^3\phi}{\sin\phi}T_{st}\frac{\partial\theta_b}{\partial\phi}\right) < f^2 a^2 \tag{1.6}$$

where T_{st} is the temperature difference between the surface and tropopause and θ_b is the boundary layer equivalent potential temperature. θ_b could further be extended to boundary layer moist static energy (MSE) [19], that is the sum of gravitational energy (Φ), thermal energy ($C_p T$, where C_p is the specific heat capacity) and latent heat (Lq, L stands for specific latent heat and q is specific humidity). Hence, positive meridional gradient of boundary layer MSE becomes a diagnostic tool of monsoon circulations, and has been tested for zonally asymmetric cases in the South Asian summmer monsoon [23]. However, the effect of baroclinic eddies on monsoon overturning circulations is still elusive due to the lack of mathematical tools.

1.3 Effects of climate change on monsoon precipitation

To quantitatively understand the response of climate change on monsoon precipitations, a current research method [24] is to perturb parameters of the moisture budget. To reduce climate model bias, a preliminary approach is to observe responses of precipitation anomalies to different climate states, then simulate the phenomena of interest into a model hierarchy and take related parameters into account so that it is clear in which hierarchy of the climate models need to improve.

Based on the method above, we first take thermodynamics factors into account to quantify climate change effect on precipitation. The simplest method uses the Clausius-Claperyon relation (CC relation), which shows that saturated water vapor pressure is proportional to air temperature. Therefore, both moisture in the air (q) and precipitation minus evaporation ($P-E$) are linearly related to the boundary layer air temperature [25]. The response of $P-E$ to varying global air temperature can be written as:

$$\delta(P-E) = \alpha(P-E)\delta T \tag{1.7}$$

where δ represents variations and α is the constant obtained from CC relation. In the case of global warming, precipitation minus evaporation variations obtained by Eq.1.7 resemble the patterns from CMIP5 model data especially in tropical areas.

To diagnose the effect from dynamical wind fields, an advanced analysis is applied by varying vertically integrated moist budget analysis as the extension of Eq.1.7 using mass conservations [26]. In the moist budget analysis, the wind velocity is usually divided into zonal average, stationary eddy and transient eddy terms. Stationary eddy terms stand for spatial deviations from zonal average and transient eddy terms represent the temporal deviations from the climatological mean. The moisture budget equation could be derived as

$$P-E \;\; = \;\; -\frac{1}{\rho g}\nabla \cdot \int_{P_S}^{P_T} q\mathbf{v}dp \tag{1.8}$$

6

where $\mathbf{v}$ is a horizontal wind vector, ρ is the density of liquid water, P_S is surface pressure, P_T is pressure at tropopause. The climatological monthly mean of the moisture budget now becomes

$$\bar{P} - \bar{E} \;=\; -\frac{1}{\rho g} \nabla \cdot \int_{P_S}^{P_T} \left(\bar{q}\bar{\mathbf{v}} + \overline{q'\mathbf{v}'} + \overline{q^*\mathbf{v}^*} \right) dp \tag{1.9}$$

where $'$ denotes stationary eddies and * transient eddies.

The effect of climate change on the moisture budget analysis could be obtained by perturbing Eq.1.9,

$$\delta(\bar{P} - \bar{E}) = -\frac{1}{\rho g} \left[\delta \int_{P_S}^{P_T} \nabla \cdot (\bar{q}\bar{\mathbf{v}}) dp + \delta \int_{P_S}^{P_T} \nabla \cdot (\overline{q'\mathbf{v}'}) dp \right.$$
$$\left. + \delta \int_{P_S}^{P_T} \nabla \cdot (\overline{q^*\mathbf{v}^*}) dp + \delta(q_s \mathbf{v_s} \cdot \nabla P_s) \right] \tag{1.10}$$

where q_s, $\mathbf{v_s}$, and P_s are specific humidity, wind, and pressure at surface level. By analyzing CMIP5 data using this method, stationary eddy terms were found to govern distributions of mid-latitude precipitations over North American regions [27] and transient eddy terms have strong response to global warming in the storm tracks [26].

The meridional gradient of MSE is closely related to monsoon circulations [19]. Thus, the budget analysis of MSE is also applied to study the monsoon onset. The MSE budget in steady state can be written as

$$\int_{P_T}^{P_S} \nabla \cdot (M\mathbf{v}) \frac{dp}{g} = F_S - F_T \tag{1.11}$$

where $M = \Phi + C_P T + Lq$ is MSE, F_T is the total energy flux at the tropopause, and F_B is the total energy flux at the surface level. Since Hadley circulations could be divided into poleward transport at the upper branch and equatorward transport at the lower branch, the MSE budget (Eq.1.11) could be approximated into two vertical layers with identical amounts of meridional wind velocity in each layer [28]. Eq.1.11 can be rewritten as

$$-\Delta M \nabla \cdot v_2 + \int_{P_T}^{P_S} \mathbf{v} \cdot \nabla M \frac{dp}{g} = F_S - F_T$$

$$\nabla \cdot v_2 = \int_{P_M}^{P_S} \nabla \cdot \mathbf{v} \frac{dp}{g} = -\nabla \cdot v_1$$

$$M_2 = \int_{P_M}^{P_S} M \nabla \cdot \mathbf{v} \frac{dp}{g} (\nabla \cdot v_2)^{-1}$$

$$M_1 = \int_{P_T}^{P_M} M \nabla \cdot \mathbf{v} \frac{dp}{g} (\nabla \cdot v_1)^{-1}$$

$$\Delta M = M_1 - M_2 \tag{1.12}$$

where 1 denotes the top layer, 2 denotes the bottom layer, P_M is the pressure at mid-level. The gross MSE (ΔM), which is the difference between two layers, indicates the vertical statbility of air flows. Varying gross MSE equation (Eq.1.12) in response to different climate forcing can be also applied to study the shift of ITCZ at upward branches of the Hadley circulations both with extra-tropical [29] and paleoclimate orbital forcing [30, 31]. Also, CMIP5 simulations using RCP 8.5 scenario also show the enhancement of gross MSE during monsoon onset periods in global monsoon areas, and this fact indicates that the delay of monsoon onset given the increase of vertical stability [32] is likely due to the delayed response of SST to the seasonal cycle due to the change of mixed layer depth [33]

Due to the lack of completeness of baroclinic eddy theories, the dynamical effect of climate change on the Hadley circulation is not as well understood as the thermodynamical effects. A key unsolved question is how meridional temperature gradients are modified by different thermal forcing, especially for paleoclimate [34] in the presence of baroclinic eddies. The meridional temperature gradient influences the strengths and positions of westerlies [35], which further affect the upward branch of the Hadley circulations. One of us [36] also observed an abrupt shift of the westerly positions during Last Glacial Maximum using transient Laboratoire de Météorologie Dynamique (LMDZ) model simulations. However, it is difficult to obtain robust answers since the strengths and locations of existing jets are very sensitive to model parameters such as surface frictions [37].

1.4   North American hydroclimate during LGM

In this section, we introduce several studies about the responses of precipitation patterns to LGM forcing. It is anticipated that many regions in North America will experience a rapid change of the hydrological cycle over the coming century based on global warming scenarios [38] from simulations of Climate Model Inter-comparison Project 5 (CMIP5). However, significant disagreements among CMIP5 models make assessing the exact magnitudes and distributions of precipitation change a challenge, especially for marginal semi-arid areas in western North America. One way to evaluate the ability of climate models to capture these changes is to run simulations under past cold climate intervals, such as the Last Glacial Maximum (LGM) 20ka ago, and compare changing patterns with geological records.

Geological records during LGM including estimations of pluvial lake shorelines [39, 40], speleothem-based reconstructions [41, 42], and pollen-based reconstruction as precipitation proxies [10] reveal increasing precipitation around most of western North America, especially the Great Basin, during LGM but decreasing precipitation in neighboring areas. This spatial pattern of the paleo-precipitation wetting-drying trend has been characterized as a "dipole" [43, 42, 44]. Several explanations have been proposed to explain the moistening trend in the Great Basin and the American southwest during LGM. Firstly, the increasing precipitation in western North America can be attributed to the southward displacement of jet streams, as the winter storm tracks, are deflected by the Laurentide Ice Sheet [45, 46]. A plausible mechanism to explain the zonally asymmetric moistening trend is the intensification of the Aleutian Low during LGM that induces the southward displacement of the atmospheric river, which is one major source of moisture for winter precipitation in California [36]. However, these works focus more on the wintertime climatology instead of studying the synoptic changes of LGM precipitation.

Several theoretical approaches have been proposed to study the synoptic change of precipitation by applying a moisture budget analysis, which quantifies the roles of precipitation, evaporation and transport in moisture conservations. The transport of moisture could be further decomposed into stationary (synoptic change) and transient (weekly or shorter time

9

scale) [26, 47, 27]. The pattern of moisture change during summertime LGM in the US has been shown to be similar to the stationary transport of moisture [47]. Model simulations also indicate strong influence of stationary waves in north American hydrological cycles during LGM [48, 49, 50, 51].

A challenge to identify the primary driver of LGM moistening of the Great Basin and the southwestern US is that the mechanisms listed above also interact with each other. For instance, the weakening NASM could be induced by decreased ventilation due to the cold air advected from the southward displacement of the jet streams [52] and increased Laurentide ice-albedo [53].

1.5   Topographic stationary waves and baroclinic instability

In this section, we briefly introduce mid-latitude wave dynamics of stationary and transient eddies. Mid-latitude stationary waves could be generated by several sources such as zonally asymmetric topography, diabatic heating, transient eddy heating, and vorticity flux [54]. However, since stationary waves formed by different sources are usually added together, it is difficult to identify the primary mechanism that contributes to the observed stationary waves. One way to differentiate the sources of stationary waves is to compare those stationary waves to the waves by climate model simulations with the additions of specific wave sources. The other method to trace the wave sources is to apply fluxes of wave activities [55, 56, 57]. Here, we will introduce a linear theory of topography forced stationary waves and wave activity fluxes that are applied to our studies.

We also introduce linear theories of baroclinic instability that is the major source of the synoptic waves in the Earth's mid-latitude atmosphere. Baroclinic instability occurs when meridional temperature gradient is greater than a critical value with strong mid-latitude jet streams at a certain pressure level. Synoptic Rossby waves initiate due to this instability and propagate eastward. Those Rossby waves keep growing due to the baroclinic instability and then deform due to the meridionally varying jet streams. The deformation of those waves causes anti-cyclonic motions in the mid-latitude and is usually called wave breaking

[58]. Synoptic Rossby waves formed by baroclinic instability also lead to the propagations of atmospheric rivers, which deliver moisture to mid-latitude regions in East Asia and North America. Hence, we speculate that the baroclinic waves are associated to the monsoon overturning circulations and precipitation.

1.5.1 A linear theory of topographic stationary waves

Topographic stationary waves form due to the conservation of potential vorticity (PV), which decreases as the shrinking depth when air flows across mountains. However, air flows usually turn northward before reaching a mountain, and this fact indicates a phase shift of topographic stationary waves. A simple, linear, and barotropic theory is developed [2] using the vorticity equation to quantify topographic stationary waves and could successfully explain the phase shift of these waves. The conservation of vorticity in a steady state consists of the vorticity advection, the Coriolis force, the surface drag, and the topographic forcing,

$$U\frac{\partial \zeta'}{\partial x} + \beta v' = -r\zeta' - \frac{fU}{H}\frac{\partial h_T}{\partial x} \tag{1.13}$$

where U is the zonally-mean zonal wind, ζ' is the zonal anomaly of vorticity, β represents a beta-plane approximation, v' is the zonal anomaly of meridional wind, r is surface drag, f is the Coriolis number, H is the scale height, and h_T is the surface topography. Assuming the surface topography has the form

$$h_T = Re[h_0 \exp(ikx)] \cos ly \tag{1.14}$$

where h_0 is the height of the mountain, k is the zonal wavenumber, and l is the meridional wave number. Hence, the solution of vorticity, as the laplacian of stream function (ψ', where $\zeta' = \nabla^2 \psi'$), becomes

$$\psi' = \frac{\tilde{h}}{(K^2 - K_S^2 - i\epsilon)} \exp(ikx) \cos ly \tag{1.15}$$

where $K^2 = k^2 + l^2$, $K_S^2 = \frac{\beta}{U}$, $\tilde{h} = \frac{fU}{H}$, and $\epsilon = \frac{rK^2}{Uk}$. We take the x derivative of ψ' to obtain v'. One typical Charney-Eliassen solution takes $K = K_S$ and the surface drag tilts

11

stationary waves by 1/4 cycle of the mountain. The magnitude and direction of topographic stationary waves near the surface can be determined by perturbations of the heat budget. Here is the rearrangement of the equation (see detailed derivations in [59]),

$$v' = -\frac{\bar{u}}{\cos\phi}\left(\frac{\partial\bar{\Theta}}{\partial\phi}\right)^{-1}\frac{\partial}{\partial x}\left(\frac{\partial\bar{\Theta}}{\partial z}h_T + \Theta'\right)$$ (1.16)

where Θ is potential temperature, and z is geo-potential height. From this equation, factors that controls stationary eddies are strength of zonal wind, meridional temperature gradient, and topography.

1.5.2   Linear theories of baroclinic instability

Linear theories of baroclinic instability are derived from the first order perturbation of vorticity equations in the geostrophically balance state, and the equation of this perturbation is called "quasi-geostrophy". Given the complexity of the atmosphere, theories with analytical solutions rely on "elegant" approximations, and here we introduce two typical models: the Eady model [3] and two-layer quasi-geostrophic (QG) model [4] given their simplicity of mathematics. Both models assume a uniformly stratified atmosphere with the same amount of vertical wind shear of zonal wind (U). The Eady model uses a continuous vertical axis with rigid surfaces and top layers, and two-layer QG model divides a vertical axis into two layers. The Eady model assumes a constant vertical zonal wind shear with height and no β effect, which is unrealistic in the mid-latitude atmosphere but the assumptions greatly simplify the mathematics.

The QG equation in the Eady model can be written as

$$\left(\frac{\partial}{\partial t} + \lambda z\frac{\partial}{\partial x}\right)\left(\nabla^2\psi' + \frac{H^2}{L_d^2}\frac{\partial^2\psi'}{\partial z^2}\right) = 0$$ (1.17)

where λ is the constant wind shear ($U = \lambda z$), H is the depth of atmosphere, and L_d is the Rossby radius of deformation, which measures the characteristic size of baroclinic eddies. The stream function can be written as

$$\psi' = \Phi(z)\sin ly\, \exp^{ik(x-ct)}$$ (1.18)

12

where k and l are zonal and meridional wavenumber, and c is the phase speed. We skip the derivations (see details in [3]) that lead to the dispersion relation

$$c = \frac{U}{2} \pm \frac{U}{\mu} \left[\left(\frac{\mu}{2} - \coth \frac{\mu}{2} \right) \left(\frac{\mu}{2} - \tanh \frac{\mu}{2} \right) \right]^{1/2} \tag{1.19}$$

where $\mu^2 = L_d^2 (k^2 + l^2)$. Baroclinic instability occurs when $\frac{\mu}{2} < \coth \frac{\mu}{2}$.

The QG equations for two layers could be written as

$$\frac{\partial q_i'}{\partial t} \quad + \quad U_i \frac{\partial q_i'}{\partial x} + v_i' \frac{\partial Q_i}{\partial y} = 0$$
$$Q_i \quad = \quad \beta y + k_d^2 U_i y \tag{1.20}$$

where $q_i' = \nabla^2 \psi_i'$ is the quasi-geostrophic PV, $k_d = \sqrt{8}/L_d$, and $i = 1, 2$ denotes the number of layers with $U_1 = -U_2 = U$. The stream function is

$$\psi_i' = \tilde{\psi}_i \sin ly \, \exp^{ik(x-ct)} \tag{1.21}$$

where $\tilde{\psi}_i$ states the wave amplitude. Hence, the dispersion relation is

$$c = -\frac{\beta}{K^2 + k_d^2} \left\{ 1 + \frac{k_d^2}{2K^2} \pm \frac{k_d^2}{2K^2} \left[1 + \frac{4K^4(K^4 - k_d^4)}{k_\beta^4 k_d^4} \right]^{1/2} \right\} \tag{1.22}$$

where $k_\beta = \sqrt{\beta/U}$, and the instability occurs when $U > \beta/k_d^2$.

1.5.3   Wave sources

A simple way to trace the sources of stationary waves is to apply the barotropic vorticity equation with only the advection of vorticity [55],

$$\frac{\partial \zeta}{\partial t} + \mathbf{v} \cdot \nabla \zeta + \zeta \nabla \cdot \mathbf{v} = 0 \tag{1.23}$$

where ζ here is absolute vorticity for simplicity. Helmholtz decompostion allows us to divide $\mathbf{v}$ into the component of divergent wind ($\mathbf{v}_\chi$) and rotational wind ($\mathbf{v}_\psi$) so that $\mathbf{v} = \mathbf{v}_\chi + \mathbf{v}_\psi$. Eq. 1.23 could be rewritten as

$$\left(\frac{\partial}{\partial t} + \mathbf{v}_\psi \cdot \nabla \right) \zeta = -\nabla \cdot (\mathbf{v}_\chi \zeta) = S \tag{1.24}$$

13

so that S is defined as the source of Rossby stationary waves, as the divergence of absolute vorticity flux.

In the Earth's atmosphere in mid-latitudes, wave sources are mainly at the order of quasi-geostrophy, which is the first order perturbation of geostrophic flows, and could be quantified by quasi-geostrophic equations. Hence, we rewrite the vorticity equation as

$$\left(\frac{\partial}{\partial t} + U\frac{\partial}{\partial x}\right)q' + v'\frac{\partial Q}{\partial y} = s' \tag{1.25}$$

where Q is zonally averaged quasi-geostrophic PV, and s' stands for quasi-geostrophic wave sources. For the steady state flow, the meridional flux of quasi-geostrophy $(v'q')$ would be conserved without external wave sources (s'). Therefore, the wave activity flux could be written as a three dimensional vector $s'q' - v'q'\frac{\partial Q}{\partial y}$, to locate the wave sources [56] and the flux is usually called Plumb flux

$$F = \frac{1}{2}p\begin{pmatrix} \left(\frac{\partial \psi'}{\partial x}\right)^2 - \psi'\frac{\partial^2 \psi'}{\partial x^2} \\ \frac{\partial \psi'}{\partial x}\frac{\partial \psi'}{\partial y} - \psi'\frac{\partial^2 \psi'}{\partial x \partial y} \\ \frac{f^2}{N^2}\left(\frac{\partial \psi'}{\partial x}\frac{\partial \psi'}{\partial z} - \psi'\frac{\partial^2 \psi'}{\partial x \partial z}\right) \end{pmatrix} \tag{1.26}$$

where F is the Plumb flux. Given the fact that mid-latitude eddies contain orders higher than QG due to Rossby wave breakings, the more advanced wave activity flux has been derived [57] by collecting all of the eddies that deviate from geostrophic balance. This "local" wave activity (LWA) could obtain the nonlinear wave activity that is unable to be quantified by the Plumb flux.

In chapter 2, we present our discovery quasi-stationary atmospheric rivers (QSARs) in north Pacific/Atlantic and identify their implications for monsoon onset. In chapter 3, we try to argue that QSARs are actually the quasi-stationary baroclinic waves and identify the sources of these stationary waves. In chapter 4, we apply wave dynamics to study precipitation in North America during LGM, and perform PMIP3 model data constraints.

CHAPTER 2

North Atlantic and Pacific quasi-stationary atmospheric rivers (QSARs) and their implications for EASM onset

Using a global space-time diagram of column water vapor (CWV) at 30°N latitude from daily reanalysis data, we find two quasi-stationary parts of atmospheric rivers (QSARs) that feature locally enhanced CWV and evolve from the Eastern Pacific/Atlantic basins in the winter to the Western Pacific/Atlantic in the summer. East Asian Summer Monsoon (EASM) onset coincides with the time CWV in the Pacific QSAR first exceeds 40 mm, which also typically occurs just before it makes landfall. QSARs exist in 39-year (1979-2017) daily climatological CWV, demonstrating the seasonal cycles of these features are quasi-stationary and potentially useful for monsoon onset prediction. EASM onset is particularly predictable following El Niño Southern Oscillation (ENSO), consistently occurring 25-40 days after the QSAR crosses the dateline.

We take a purely empirical approach to investigate the mechanisms that link ocean basins with monsoon onset. Using a longitude-time Hovmöller diagram of column water vapor (CWV) at 30°N in daily ERA-Interim reanalysis [9], we identify regions of enhanced CWV in the Pacific and Atlantic Ocean basins that coincide with the climatological crossing-points of quasi-stationary atmospheric rivers at 30°N; we term these quasi-stationary parts of atmospheric rivers (QSARs). We identify QSARs in the Hovmöller diagrams of CWV in section 2.1 and clarify their phenomonological patterns in section 2.2 We compare with the EASM onset index in section 2.3 and quantify the influence of El Niño Southern Oscillation (ENSO) in section 2.4.

15

2.1 QSAR: Zonally and seasonally migrating local CWV maxima in the Pacific/Atlantic

We show a global longitude-time (Hovmöller) plot of CWV at 30°N in 2017 using daily-mean ERA-Interim reanalysis in Fig. 2.1a. 30°N was particularly chosen to investigate the extensions of monsoons outside typical ITCZ migrations and further into the subtropics, especially in East Asia. Several types of CWV patterns could be found in Fig. 2.1a: summer (mid June–mid October) CWV enhancement in the Pacific (120°E-120°W) and Atlantic (90°W-10°W), low CWV values especially at the Tibetan Plateau (80–100°E) and Rocky Mountains (105–110°W) for the entire year (as illustrated in Fig. 2.1a), a series of synoptic eastward-propagating waves (pointed to by red arrows in Fig. 2.1a) downstream of the Tibetan Plateau and Rocky Mountains during winter and spring (November–June), and two seasonally migrating bands with local, zonal maxima of CWV in both the Pacific and Atlantic basins (black-white curves in Fig. 2.1a).

We now focus on the two seasonally migrating bands; these correspond to the quasi-stationary parts of atmospheric rivers (QSARs; see section 2.3 for details). To identify the pathways of QSARs, it is insufficient to simply define discrete QSAR pathways as longitudes containing local CWV maxima within their own ocean basins because those maxima sometimes occur at synoptic eastward-propagating waves instead of QSARs. Hence, we develop a feature-tracking algorithm to find local CWV maxima in a given longitude range (see section 2.1.1 for more details), with which we identify QSAR pathways (black/white curves in Fig. 2.1a/2.2a). As shown in Fig. 2.1a/2.2a, QSAR pathways emerge from eastern-central Pacific/Atlantic during wintertime (January to April) and then start to propagate westward (mid April for Pacific QSAR/mid May for Atlantic QSAR). The Pacific QSAR reaches the western boundary of the Pacific about the time of EASM onset (yellow stippling; see section 2.4 for details), and returns to the east roughly when EASM concludes.

QSARs exist but appear smoother in a 5-year (2012-2017) daily climatology of CWV (Fig. 2.3). Even in the 39-year (1979-2017) climatological mean CWV at 30N (Fig. 2.2b), two QSARs can still be identified in the Pacific and Atlantic Ocean basins respectively

by applying the tracking algorithm on the 39-year climatological CWV, although they are less prominent compared to an individual year (Fig. 2.2a) and 5-year climatological mean (Fig. 2.3). The presence of QSARs in the long-term, daily climatology indicates these features are quasi-stationary phenomena with a seasonal cycle. QSARs are also apparent in satellite CWV (Fig. 2.4), for all latitudes between 25°N to 40°N, albeit with slightly different pathways. This fact indicates that QSARs are involved in large-scale atmospheric flow spanning of 25°N to 40°N.

2.1.1 Method for identifying QSAR pathways

Given the possibility of QSARs as monsoon predictors, one requisite task is to identify the pathway of QSAR propagations. However, due to the noisiness of raw data, a simple tracking of the local maximum CWV in each ocean basin is discontinuous, and fails to represent smooth QSAR pathways that the eye easily picks out in Fig. 2.1a/2.1b. Therefore, we develop a technique to generate continuous pathways of QSARs. First, a QSAR begins at the location with maximum CWV inside Pacific (120°E-120°W) and Atlantic (90°W-10°W) on January 1st. Each subsequent day, a QSAR is defined to be at a neighboring location where the CWV is locally maximal. The neighbor location is chosen at the appropriate window of a longitudinal range. A narrow window size is inflexible enough to follow QSARs but a wide window captures large amounts of synoptic structures of ARs.

We test several pairs of window sizes that generate QSAR pathways (as shown in Fig. 2.5a), and list the percentage of days with local maxima occurring at the window edge in Table 2.1, to find the window sizes that better identify reasonable QSAR pathways for this study. A reasonable percentage is the window that is wide enough to not have too many edge maxima while minimizing the number of jumps due to synoptic events; we settled on ∼ 50%. Hence, we choose 6.75°W-5.25°E of the Pacific window and 3.75°W-4.5°E of Atlantic window. To evaluate the significance of those pathways, we generate 1000 pathways (as shown in Fig. 2.5b) by adding white noise to the raw CWV with an amplitude ratio of 0.4 relative to the variance of the data, and plot their ensemble averages. The chosen noise
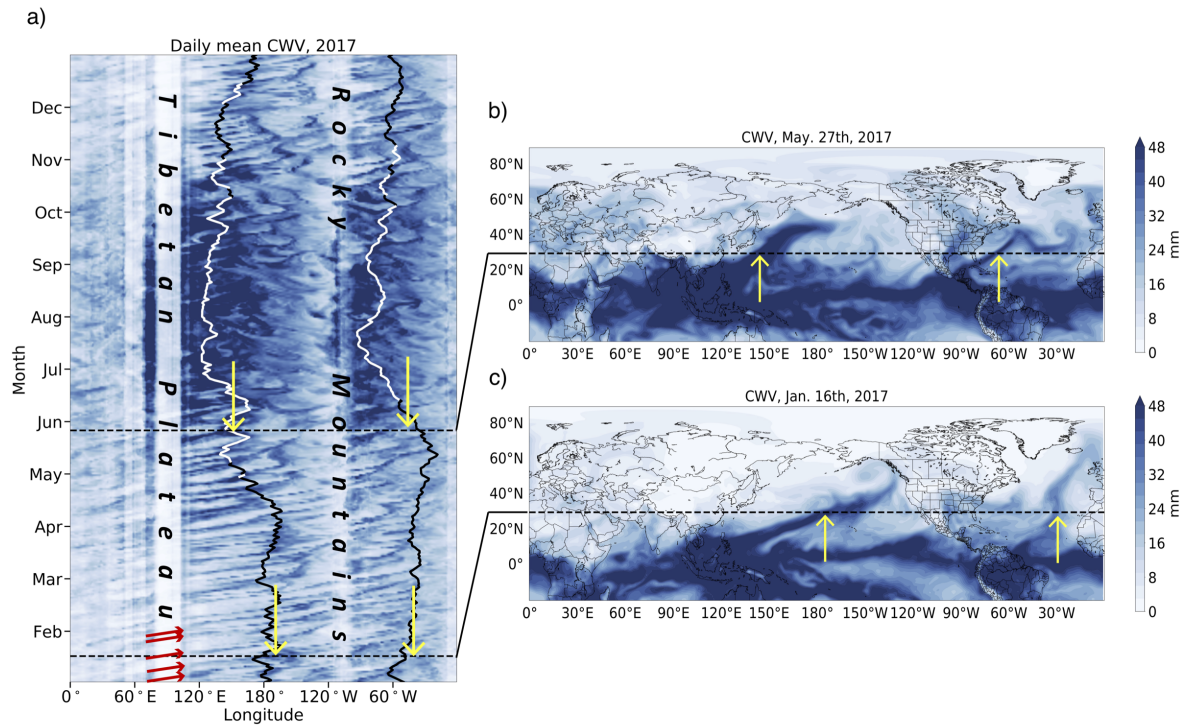
Figure 2.1: **a**. Hovmöller diagram of CWV (2017) at 30°N with the addition of (1) QSAR pathways marked by white curves (with the amount of 7-day moving averaged CWV above 40 mm) and black curve (below 40 mm), (2) red arrows to illustrate synoptic westerly waves, (3) two black dashed horizontal lines and yellow arrows to show the locations of QSARs on May 27th, 2017 and January 16th, 2017. **b**. CWV map on May 27th, 2017. The black dashed horizontal line shows 30°N and two yellow arrows indicate the locations of QSAR observed in **a**. **c**. Same as **b**, but on January 16th, 2017.
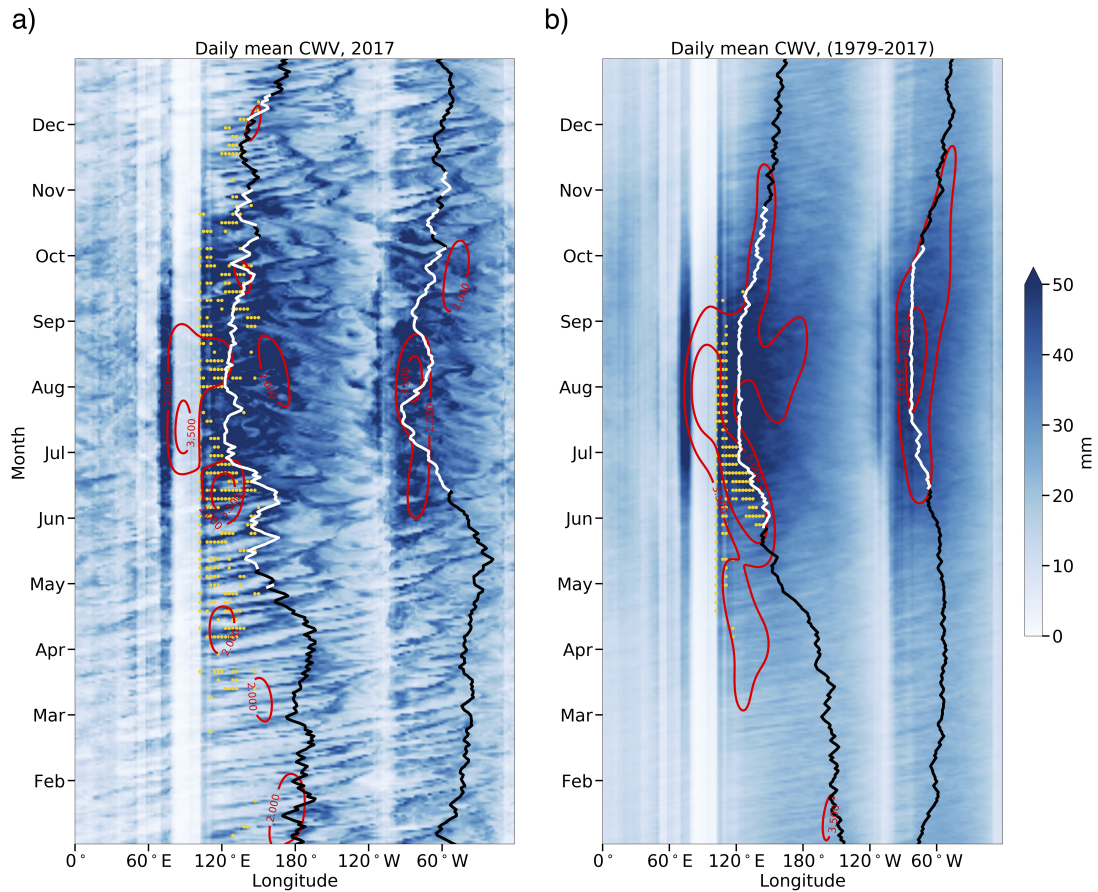
Figure 2.2: **a**. Hovmöller diagram of CWV (2017) at 30°N with the addition of QSAR pathways marked by white curves (with the amount of 7-day moving averaged CWV above 40 mm) and black curve (below 40 mm). Yellow stippling indicates areas that satisfy the monsoon index and the red contours are smoothed precipitation (mm/d). **b**. Same as **a**., but for 39-year (1979-2017) climatological mean.
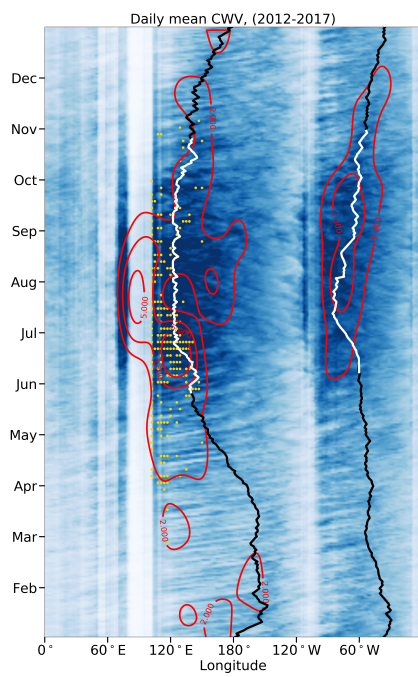
Figure 2.3: Same as Fig. 2.2a., but for 5-year (2012-2017) climatological mean.
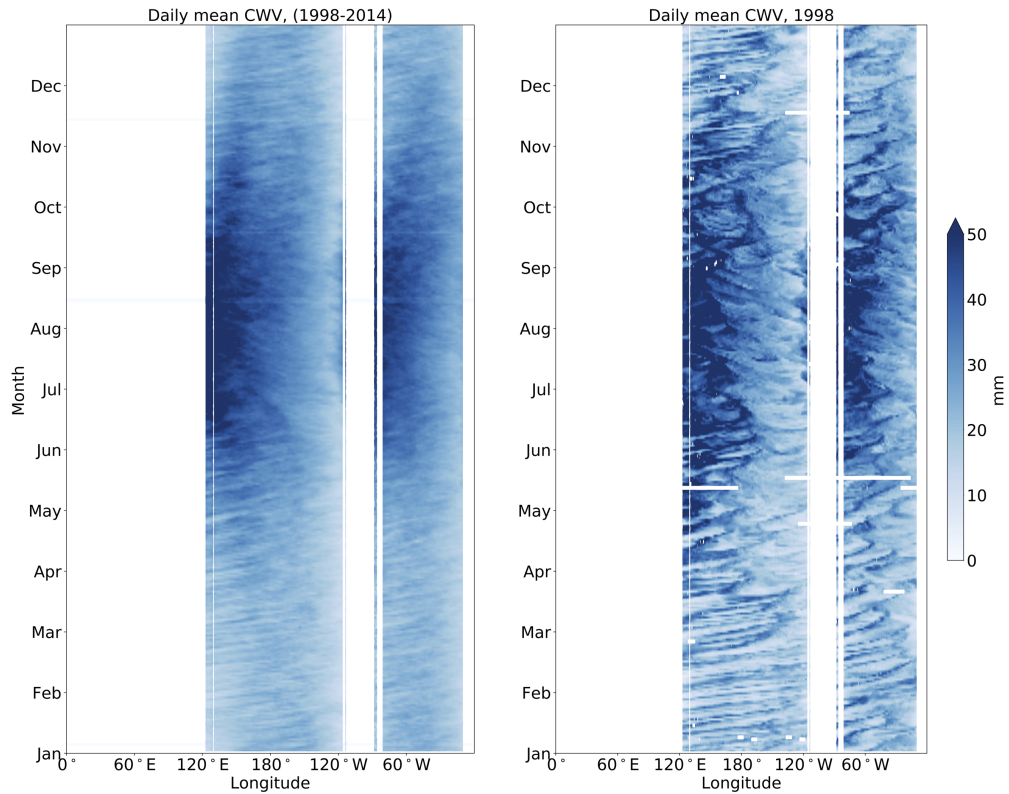
Figure 2.4: (Left) Hovmöller diagram of CWV in climatology mean (1998-2014) and (right) in 1998 using Tropical Rainfall Measuring Mission's (TRMM) Microwave Imager (TMI) data. The QSARs are displayed the same as reanalysis data. However, to obtain more statistical analysis (1979-2017), we used ERA-Interim data.

ratio has been tested to optimize identification of QSAR pathways, and contains the same order of standard deviations ($\sim$10° of longitudes) due to the different window sizes.

The majority of QSARs stay at the same longitude during summertime (July-September), because CWV loses its continuity due to large topography, especially in East Asia. Therefore, when calculating a QSAR pathway, we exclude the East Asian continent (west of 123°E) to prevent the Pacific QSAR from staying in East Asia after monsoon retreats. The one-month convergence of Pacific QSARs beginning at each longitude of 150°E-120°W on January 1st (as shown in Fig. 2.5c) indicates that the tracking algorithm could tolerate a certain range of different initial locations. QSAR pathways on 5-/39-year climatological CWV could be acquired by applying the same algorithm on daily climatological average of CWV. QSAR pathways are unnecessary to be closed at the start/end date (January 1st/December 31st) for individual year and ENSO climatology, but need to be closed at the start/end date for 5-year and 39-year climatology. To ensure an enclosed QSAR pathway, we set two consecutive climatological annual cycles, initiate the tracking algorithm on January 15th in the second year, run for both subsequent/preceding days forward/backward to deep summers, and form the annual cycle of a QSAR pathway between two summers.

2.1.2   The sensitivity test of different window sizes, and the dateline crossing date

The QSAR tracking algorithm can be viewed as a low-pass filter especially for narrow window sizes. Since the typical size of an AR is about 3-5° in longitude, those fluctuations that have been filtered out are mainly inside the range of a QSAR. Hence, the tracking algorithm intrinsically smoothens QSAR pathways by filtering out inherent fluctuations inside QSARs.

The window size sensitivity of QSAR pathways could be reduced from 10° to 5° in longitude and the number of multiple crossing of the dateline by applying the tracking algorithm on 7-day running mean of CWV data. However, it also enhances the uncertainties of QSAR pathways by 7 days, and reduces the resolutions of QSAR pathways especially during monsoon onset periods. For example, the predicted QSAR pathway using daily CWV

a) 2017, QSAR paths with different windows

b) 2017, QSAR paths with noises

c) 2017, QSAR paths with different initial values
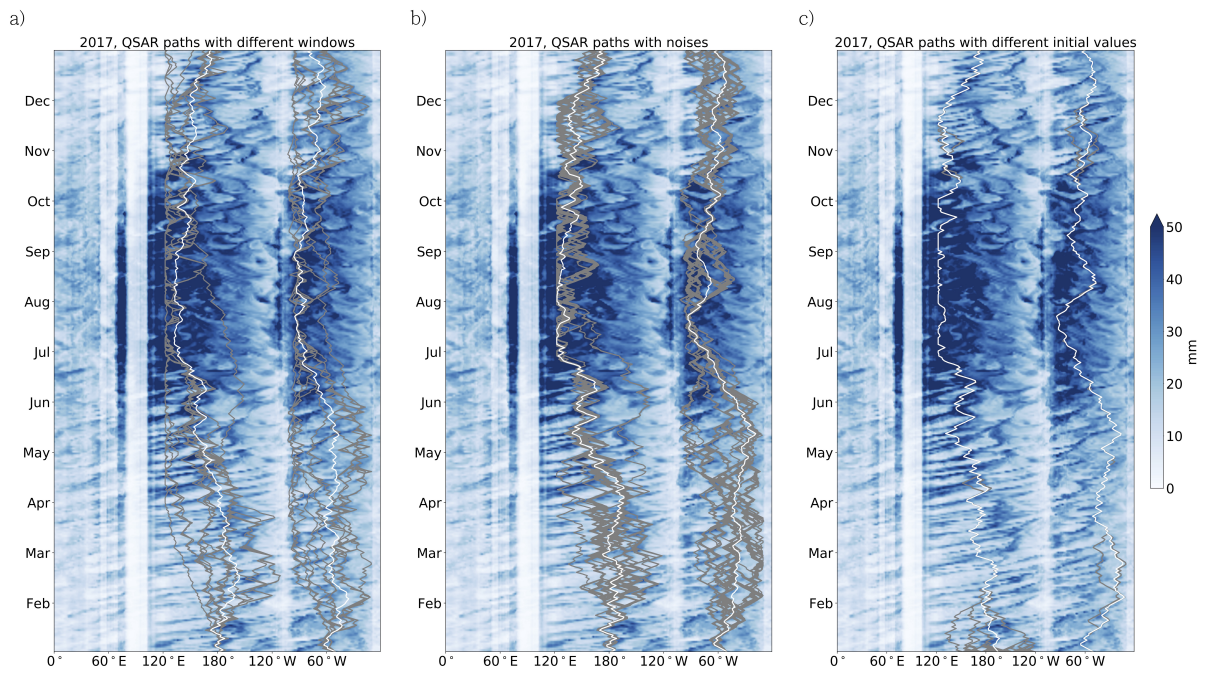
Figure 2.5: **a**. Hovmöller diagrams of CWV (2017) with simulated QSARs (grey curves) using different pairs of window sizes and their ensemble averages (white curves). **b**. Same as **a**., but for one thousand realizations by adding white noise to the raw CWV. **c**. Same as **a**., but for different initial longitudes of Pacific.

Table 2.1: The percentages of days with CWV local maxima occurring at window edges with different pairs of window sizes. °W/°E stands for a window size west/east of QSAR pathways at the previous day.

°W	°E	percentages (Pacific)	percentages (Atlantic)
2.25	2.25	68.8	57.3
2.25	3	68.2	61.6
3	2.25	65.5	55.1
3	3	63.0	52.9
3	3.75	60.8	51.8
3.75	3	56.7	45.8
3.75	3.75	55.1	51.8
3.75	4.5	55.9	50.1
4.5	3.75	54.8	41.1
4.5	4.5	53.7	41.4
4.5	5.25	51.0	39.7
5.25	4.5	54.8	38.1
5.25	5.25	51.0	39.5
5.25	6	49.6	34.2
6	5.25	46.3	36.2
6	6	43.8	30.1
6	6.75	42.5	28.5
6.75	6	41.4	30.4
6.75	6.75	38.9	27.1
6.75	7.5	37.8	26.3
7.5	6.75	41.4	27.4
7.5	7.5	38.4	24.4
7.5	8.25	36.7	20.8
8.25	7.5	37.3	24.7
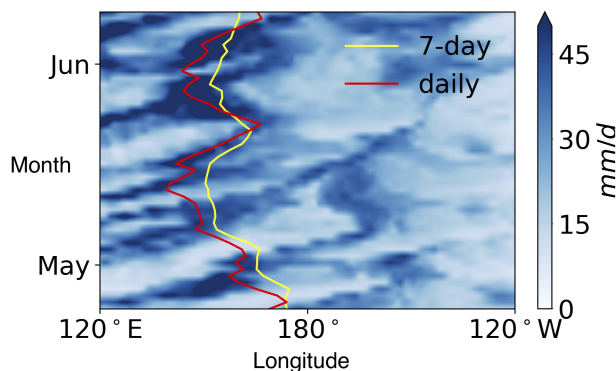
Figure 2.6: Hovmöller diagram of CWV (2017) at 30°N with the QSAR pathway identified for daily CWV (the red curve) and the QSAR pathway for 7-day running average CWV (the yellow curve).

is closer to the eye-catching QSAR than the one using 7-day running mean CWV during mid-May, 2017 (Fig. 2.6). Hence, the QSAR pathway determined by 7-day running mean CWV blurs the exact EASM onset date. The usage of running mean with larger time period trades the accuracy of QSAR pathways and monsoon onset dates for lower window size sensitivities and numbers of multiple dateline crossings. To achieve a single QSAR dateline crossing requires performing the tracking algorithm on running mean CWV data for more than 7-days, and this further blurs the EASM onset date. Therefore, we avoid taking time mean of the data, and try to develop the dateline crossing index by only averaging over area.

Hence, this dateline crossing date index was constructed based on the fact that the migrations of QSAR cause zonal anomalies of Pacific CWV. During wintertime, the Eastern Pacific contains relatively larger CWV than the Western Pacific. As the QSAR moves into the Western Pacific in summer, the CWV is larger in the Western Pacific than in the Eastern Pacific (Fig. 2.7).

2.1.3 Technique to smooth precipitation contours in Fig. 2.1 and Fig. 2.3

The key issue to smooth precipitation contours is the influence of precipitation from surface topography in East Asia. A series of precipitation spikes occur in East Asian and North
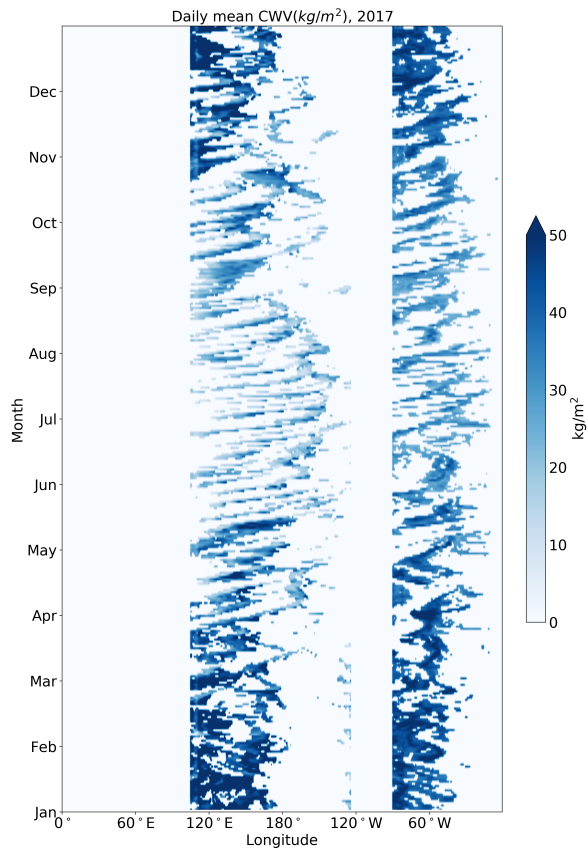
Figure 2.7: Hovmöller diagram of the Pacific CWV and Atlantic CWV (at 30°N in 2017) that are 1.15 times greater than the average CWV for each respective basin.

American continents in Fig. 2.3. Once you perform the filtering without dealing with precipitation skipes, the effect of surface topography will spread out to the neighboring areas and distort the shapes of precipitation contours, so we need to remove the spikes of precipitation. We first smooth precipitation by filtering out the signals greater than the typical spectrum of topography (~ 0.2 degree^{-1}) and then pick up the local minimum values of the curves. The final curve is obtained by cubic interpolation of each local minimum. Therefore, we can perform a special-temporal low-pass filtering (cutoff frequency 0.027 degree^{-1} in this case) to smooth precipitation. Although the technique lowers the overall average of precipitation, the spatial-temporal pattern is preserved without the strong influence of spikes.

2.2 QSAR: The quasi-stationary parts of atmospheric rivers

We have so far phenomenologically described QSARs evolving from eastern-central Pacific/Atlantic, propagating westward in the winter and spring, and making landfall during the summer monsoon. We now demostrate the propagating nature of QSARs and clarify the relation to atmospheric rivers. Atmospheric rivers are the eastward-propagating extensions of CWV filaments from deep tropics to subtropics/mid-latitudes, and are associated with synoptic eastward-propagating waves [60] in Hovmöller diagrams (illustrated by red arrows in Fig. 2.1a). The eastward-propagating waves initiate downstream of the Tibetan Plateau and the Rocky Mountains, and terminate at the Pacific/Atlantic QSARs respectively, especially during wintertime. The waves that travel upstream of the Tibetan Plateau and terminate west of the Tibetan Plateau are beyond our major interests in this study.

The global northern hemispheric CWV maps on January 16th, 2017 (Fig. 2.1c) and May 27th, 2017 (Fig. 2.1b) have particularly prominent QSARs in each basin, and we choose these dates to avoid confusion between propagating synoptic waves and QSARs. The Hovmöller diagram (Fig. 2.1a) shows that Pacific/Atlantic QSARs on January 16th, 2017 are located near the dateline and 30°W respectively (marked by two yellow arrows on January 16th) where two crossing-points at 30°N of the Pacific/Atlantic atmospheric rivers appear as the filaments containing high values of CWV extending toward mid-latitudes in the CWV map

plot for the same day (two yellow arrows in Fig. 2.1c). Similarly, locations of Pacific/Atlantic QSARs on May 27th, 2017 (marked by two yellow arrows on May 27th in Fig. 2.1a) stay at crossing-points of the Pacific/Atlantic atmospheric rivers at 30°N (two yellow arrows in Fig. 2.1b). Therefore, QSARs are actually the crossing-points of atmospheric rivers at 30°N. Given that synoptic atmospheric rivers halt at QSARs, QSARs can be regarded as where synoptic atmospheric rivers become quasi-stationary and terminate their eastward propagation.

Recent studies discovered a southerly water vapor front with intense moisture delivery to East Asia [61, 62, 63] during EASM seasons [64, 65], and determined several ENSO-induced extreme events [66]. Atmospheric rivers also contribute to the intense moisture delivery [67] with their variations in strength induced by EASM [68, 69] and ENSO [68] climatologically. Climate model simulations further indicate the roles of synoptic waves in monsoon onset [18, 19]. Hence, our study bridges the traditional view of southerly water fronts during EASM seasons with our discovery of QSARs due to the coincidence of QSARs with EASM onset in longitude-time Hovmöller diagrams from Fig. 2.2.

2.3   The implications of QSAR to EASM onset

We articulate the link between QSARs and EASM onset by ploting a widely used empirical monsoon index [6] adopted in the IPCC report [5] onto the Hovmöller diagram (Fig. 2.2a and 2.2b). The index defines monsoon periods when 5-day moving averaged precipitation is 5 mm/d greater than January averaged precipitation for each location. In Fig. 2.2b, the EASM region (marked by yellow stippling) evolves from the west Pacific (130°E-140°E) in late May (on May 31st on average) gradually toward the East Asian continent (100°E-110°E) in mid-June (on June 11th on average). Several early, individual extreme precipitation events occurring near the Tibetan Plateau in April and May also meet the monsoon index criteria, but here we ignore those events since they are outside our primary interests in this study.

The Pacific QSAR presented in Fig. 2.2b coincides with the eastern edge of the EASM region when the monsoon onset occurs over the ocean, and then propagates with the monsoon
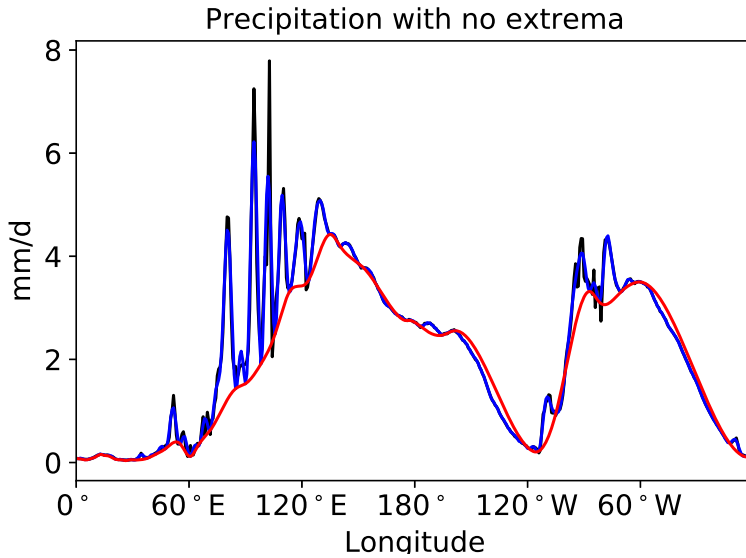
Figure 2.8: Annual mean of climatological (1979-2017) precipitation (the black curve). Primary filtering by removing high frequency(0.2 degree^{-1} in this case,the blue curve). The precipitation without spikes (the red curve).

onto land. To better interpret the relation between QSARs and the monsoon index, we plot smoothed precipitation contours (red contour in Fig. 2.2b) onto the Hovmöller diagrams (the technique we apply to smooth the precipitation contour is described in section 2.1.3; Fig. 2.8). QSAR pathways with their 7-day moving averaged CWV above 40 mm (white curves in Fig. 2.2b) roughly fit the 5 mm/d contour in the Pacific sector.

The coincidence between the 5 mm/d precipitation in monsoon regions and 40 mm CWV in composite Hovmöller plots strongly suggests that QSARs indicate moisture supply for precipitation over the areas through which they pass. This is perhaps expected, since at least tropical precipitation is tightly coupled to a threshold value of CWV (see Fig. 2.9; ref. [70]). Therefore, we define monsoon onset within the CWV dataset to occur when the QSAR value first exceeds 40 mm. In the 39-year climatology, the Pacific QSAR first exceeds 40 mm on May 29th at 144.6°E, about the same time as the monsoon onset date (May 31st) from the precipitation-based monsoon index used by the IPCC. Given that CWV fluctuates less than precipitation for individual years (Fig. 2.2a), we use the 40-mm exceedance date for the discussion of year-to-year variability.
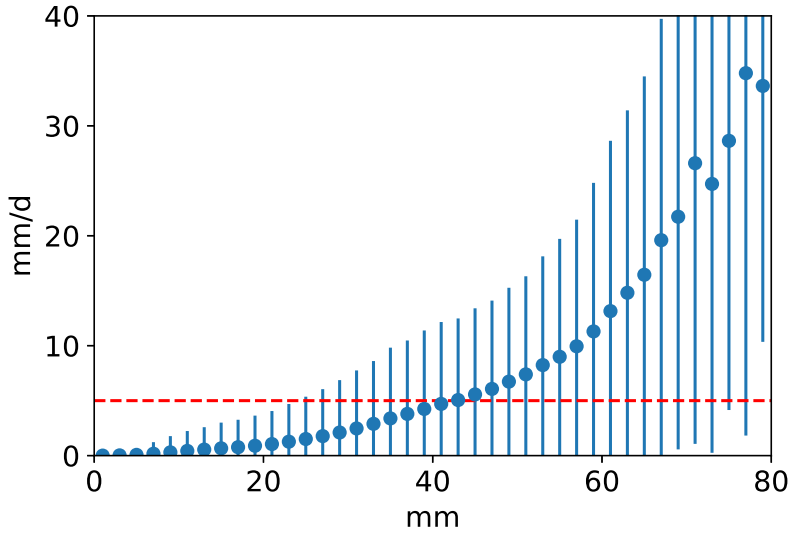
Figure 2.9: The averaged precipitations (blue dots) and standard deviations (blue error-bars) w.r.t. CWV at 30°N over global ocean basins for the past 39 years (1979-2017). The red dashed line show the 5 mm/d precipitation.

2.4 QSAR variability and EASM onset prediction

As might be expected, QSAR seasonal pathways are sensitive to Pacific climate variability, particularly ENSO. Hovmöller diagrams for El Niño and La Niña composite CWV are presented in Fig. 2.10a and 2.10b with the lists of ENSO years given in Table 2.2. During El Niño conditions, monsoon area, precipitation and QSARs behave similarly compared to the 39-year daily climatology. However, QSARs during La Niña years are more centrally located in the Pacific, while during El Niño and in the climatology, QSARs begin in the winter in the east Pacific and traverse a larger distance westward. Climatologically, QSARs reach 40 mm on May 26th (143.4°E) during La Niña and on June 3rd (136.4°E) during El Niño. These dates are also consistent with the monsoon onset dates, on May 23rd for La Niña and on June 7th for El Niño, obtained from the IPCC precipitation index. Therefore, we conclude that CWV QSARs are consistent with the earlier/delayed EASM onsets during El Niño/La Niña states, and this result is consistent with studies of climatological EASM onsets under the influence of ENSO states [71, 72, 73, 74, 75].

Similar analysis of individual-year precipitation to identify monsoon onset dates using the IPCC precipitation index fails because daily precipitation variability is similar in magnitude to the 5mm/day threshold. To identify the monsoon onset date for each year, several techniques have been developed. These include filtering the raw data using empirical orthogonal functions [76] and averaging large areas of precipitation data [77, 78], but these monsoon indices mask the fine spatiotemporal structures of the EASM. In contrast, the pathways of the QSARs and their 40 mm CWV threshold can be identified for each individual year; Fig. 2.2a shows the QSAR pathway for 2017, which has a 40-mm exceedance date of May 10. Because of the strong dependence of precipitation on CWV (Fig. 2.9), we propose to use 40-mm exceedance dates of the Pacific QSARs as a proxy of EASM onset; we perform the same technique to generate QSAR pathways during individual years and summarize 40-mm exceedance dates of QSARs for the past 39 years in Table 2.2.

We now offer a simple forecasting metric with predictive skill for the EASM onset during individual years by utilizing the passage of the Pacific QSAR across the dateline. However, Pacific QSARs might travel back-and-forth along the dateline (Fig. 2.2a) given the strong influence of synoptic westerly waves. To avoid this ambiguity, we define the dateline crossing date by requiring the mean CWV at 30 °N and 120°E-180°W to be greater than at 180°W-120°W, and for the difference to exceed three standard deviations of the historical W-E Pacific CWV difference without a climatological seasonal cycle (see section 2.1.3). This quantity is readily calculabe for each individual year and is summarized in Table 2.2. The correlation coefficient between 40mm exceedance date and dateline crossing of the QSAR for all years is 0.51 (p-value 0.001; see Fig. 2.11b), which indicates our simple CWV metric has some skill in predicting the onset of the EASM.

Fig. 2.10c/2.10d show scatter plots and linear regressions between 40mm-exceedance date and dateline crossing of the Pacific QSARs in years following El Niño/La Niña (Niño 3.4 greater/less than 0.25 in May). With this ENSO-based separation, high correlation coefficients and low p-values indicate that ENSO indeed governs the QSAR pathways and the subsequent monsoon onsets. The distinct slopes between El Niño/La Niña years can be attributed to the different types of QSAR pathways, as discussed before (Fig. 2.10a/2.10b).

31

Our analysis reveals that ENSO has an indirect influence on monsoon onset date, by determining the lead-time between dateline crossing of the Pacific QSAR and monsoon onset. During an El Niño, the linear regression indicates that with high confidence, the Pacific QSAR dateline crossing (March 22nd) occurs 40 days before EASM onset, and 25 days before onset when it occurs on May 16th. During La Niña years, the linear regression indicates 50-days lead-time between dateline crossing and EASM onset when the former occurs on March 22nd, however there is zero lead-time when the dateline crossing occurs on May 28th. As for non-ENSO years (9 over 39 years, as shown in Fig. 2.11a), the trend of dateline crossing leading EASM onset is insignificant.

The influence of ENSO on EASM onset is unable to fully doesn't year-to-year variability of EASM onset as indicated by the moderate linear correlation coefficients [78, 79], probably because the influence itself changes year-to-year [80] or other climate factors also influence the monsoon onset [81]. Our precursor of the EASM due to the seasonal pathway of the Pacific QSARs defines two distinct slopes of linear regression with higher correlation coefficients, although we have yet to establish the cause of a QSAR and how it impacts the EASM.

Table 2.2: QSAR dateline crossing dates, first 40-mm CWV exceedance dates, dateline crossing lead-dates (the negative value mean lag-date), and Niño 3.4 in May.

Year	Dateline Crossing	40-mm Exceedance	Lead-Date	Niño 3.4
1979	Jun/4	May/19	-16	0.23 Neutral
1980	Apr/13	May/15	32	0.48 El Niño
1981	Apr/5	May/14	39	-0.26 La Niña
1982	May/9	May/31	22	0.66 El Niño
1983	Apr/13	May/24	41	1.06 El Niño
1984	May/16	Jun/7	22	-0.51 La Niña
1985	May/16	May/24	8	-0.78 La Niña
1986	May/29	May/31	2	-0.12 Neutral
1987	May/7	Jun/8	32	0.97 El Niño

1988	Mar/15	May/23	69	-0.88 La Niña
1989	Apr/4	May/15	41	-0.58 La Niña
1990	May/4	Jun/11	38	0.29 El Niño
1991	Mar/26	May/10	45	0.45 El Niño
1992	Apr/28	Jul/28*	91	1.06 El Niño
1993	May/1	Jun/6	36	0.7 El Niño
1994	Apr/19	May/17	28	0.42 El Niño
1995	Apr/17	Jun/3	47	0.14 Neutral
1996	May/30	May/29	-1	-0.31 La Niña
1997	May/2	Jun/11	40	0.75 El Niño
1998	Apr/8	May/4	26	0.45 El Niño
1999	Mar/19	May/10	52	-1.02 La Niña
2000	Apr/3	May/14	41	-0.71 La Niña
2001	May/9	May/24	15	-0.25 Neutral
2002	Apr/21	May/29	38	0.43 El Niño
2003	May/5	May/9	4	-0.26 La Niña
2004	May/9	May/16	7	0.17 Neutral
2005	May/11	May/27	16	0.29 El Niño
2006	May/17	May/25	8	-0.05 Neutral
2007	Apr/24	May/26	32	-0.29 La Niña
2008	May/9	May/18	9	-0.75 La Niña
2009	Apr/20	Jun/1	42	0.09 Neutral
2010	Apr/12	Jun/3	52	-0.09 Neutral
2011	May/3	May/29	26	-0.47 La Niña
2012	May/26	May/28	2	-0.18 Neutral
2013	Mar/24	May/5	42	-0.27 La Niña
2014	May/15	Jun/5	21	0.3 El Niño
2015	Apr/30	May/17	17	1.02 El Niño
2016	Apr/6	May/7	31	0.48 El Niño

| 2017 | Apr/11 | May/10 | 29 | 0.38 El Niño |

*An outlier in 1992.

2.5   Summary

From a global Hovmöller diagram of CWV using ERA-Interim reanalysis on 30°N in 2017, we discover seasonally migrating QSARs that evolve from east Pacific/Atlantic during wintertime and travel to west Pacific/Atlantic during summertime. QSARs are also observed in Hovmöller diagrams of 5-year (2012-2017)/39-year (1979-2017) climatological mean CWV, and TRMM satellite data. We develop a tracking algorithm to identify QSAR pathways from CWV Hovmöller diagrams, and a significance test is also performed to estimate the confidence of simulated QSAR pathways. By applying the IPCC monsoon onset index, EASM onset date occurs when the Pacific QSAR CWV exceeds 40 mm. Hence, a CWV-based monsoon onset index can be constructed to predict EASM onset for each individual year. Using the CWV-based monsoon onset index, EASM onset dates could be predicted about a month in advance when the Pacific QSARs across the dateline during El Niño. The predictability of EASM onset dates is weaker during La Niña, but the linear relations between EASM onset dates and Pacific QSAR dateline crossing dates are still significant.
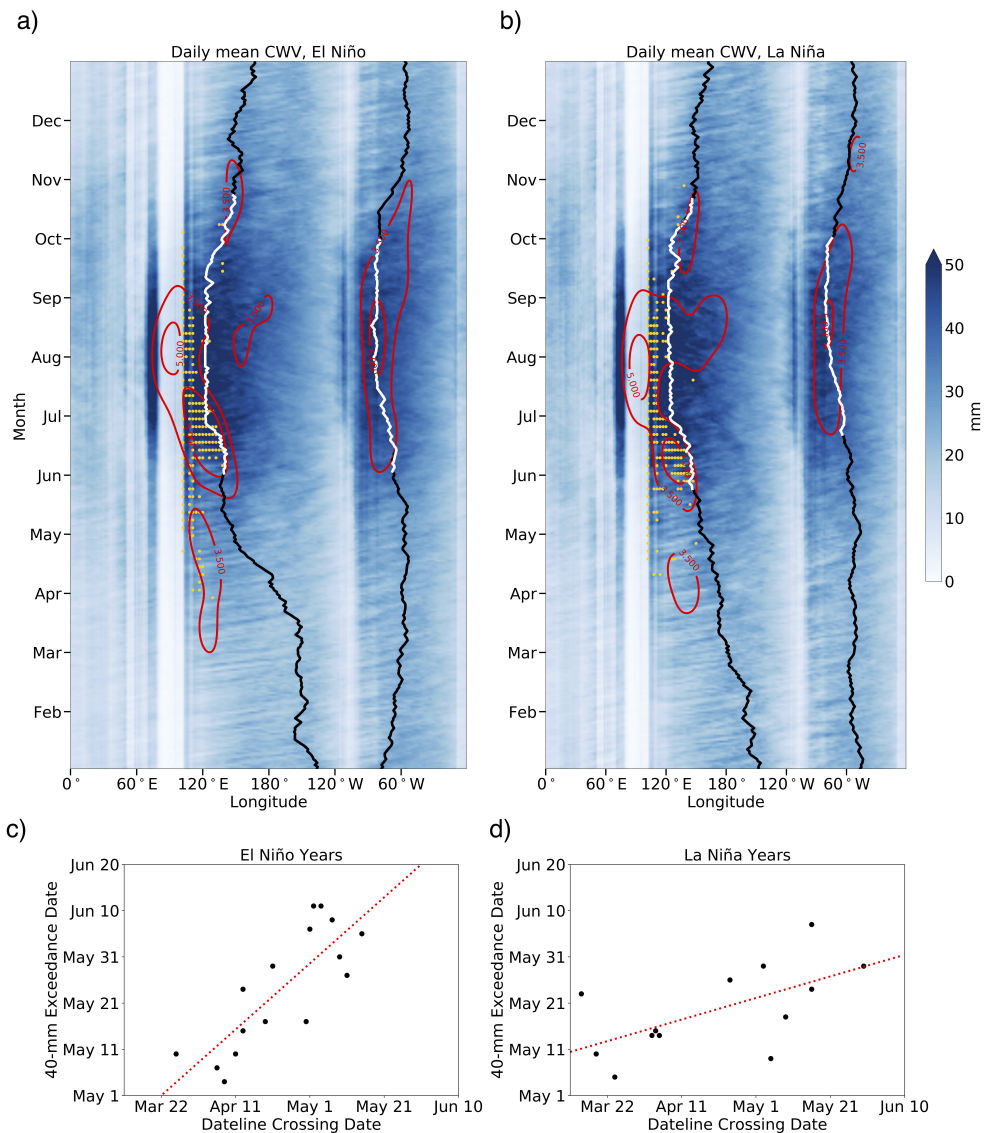
Figure 2.10: **a**. Same as Fig. 2.2 but for El Niño (decaying El Niño). **b**. Same as **a**. but for La Niña (decaying La Niña). Enclosed QSAR pathways of El Niño/La Niña are not required unlike 5-year and 39-year climatology (see section 2.1.1). **c**. The scatter plot of 40-mm exceedance date of the QSAR (our monsoon onset proxy) without an outlier in 1992, and the date when the zonal average of 30°N CWV on 180°W-120°W is greater than 120°E-180°W (dateline crossing) during El Niño with the slope 0.71, intercept 63 days, correlation coefficient 0.81, and p-value 0.0002 by linear regression analysis. El Niño years here are selected when Niño 3.4 index in May is above 0.25. **d**. Same as **c**., but for La Niña with the slope 0.23, intercept 113 days, correlation coefficient 0.61, and p-value 0.026. La Niña years here are selected when Niño 3.4 index in May is below -0.25.

35
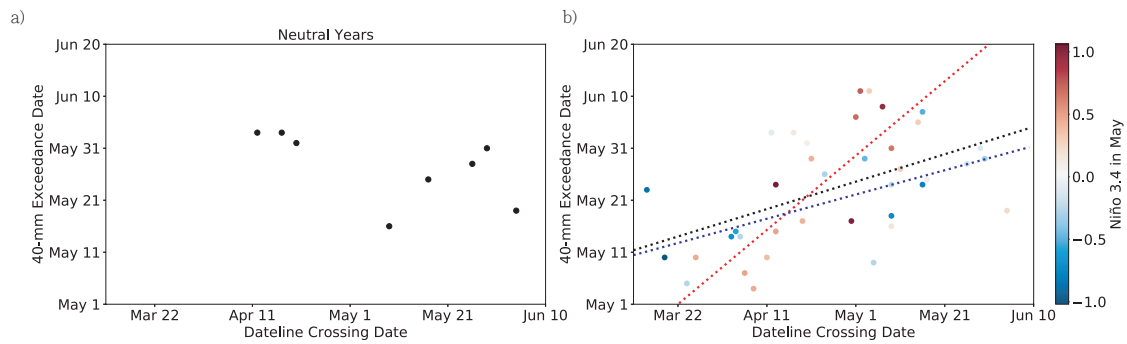
Figure 2.11: **a**. The scatter plot of 40-mm exceedance date of the QSAR, and the dateline crossing during neutral years. **b**. Same as **a**., but for entire past 39 years with the slope 0.26, intercept 112 days, correlation coefficient 0.51, and p-value 0.001 by linear regression analysis (as shown in the black line). Linear regression analysis of El Niño (the red line) and La Niña (the blue line) are added for comparison.

CHAPTER 3

QSARs: The quasi-stationary baroclinic waves?

In this chapter, we focus on dynamics of QSARs from the aspect of mid-latitude baroclinic waves. We perform a Hovmöller diagram of upper level (250mb) local wave activity (LWA, see section 1.5.3 [57]) at 30°N for the past 39 years (1979-2017). The analysis of LWA shows that Pacific/Atlantic QSARs divide each basin into two regimes since LWA largely enhances downstream of both Pacific/Atlantic QSARs, and this fact indicates that QSARs as fronts of wave breakings, thus opening a new window into dynamics of subtropical monsoon extensions. The simplified GCM simulations show that the zonally asymmetric jet streams induced by a tropical warm pool-cold tongue is a primary driver of QSARs. A possible explanation is that QSARs occur when the phase speed of baroclinic waves equals zonally decreasing jet streams due to the tropical warm pool-cold tongue. Semi-empirical baroclinic instability theories (Eady and two-layer QG models) are provided to verify that QSARs are indeed located at the quasi-stationary baroclinic waves.

In section 3.1, we present the Hovmöller diagram of upper level (250mb) at 30°N for the past 39 years (1979-2017). The simplified GCM simulations are shown in section 3.2. The plausible mechanism of QSARs with semi-empirical baroclinic theories are illustrated in section 3.3. We also provide Hovmöller diagrams of low-level (850mb) MSE and wind convergence given that two physical quantities are typical tools to diagnose the monsoon onsets (see section 1.2 for details).

3.1 QSAR: The quasi-stationary wave-breaking front

We now discuss interaction of QSARs with westerly synoptic waves that are representative of the westerly signals in Hovmöller diagrams from Fig. 2.2 as we described in section 2, and speculate on the potential mechanism that halts those waves. Westerly synoptic waves typically initiate downstream of the Tibetan Plateau and Rocky Mountains but grow in amplitude as they propagate to the east, eventually breaking and decaying in about 8 days [58]. The wave breaking occurs when westerly synoptic waves fold back on themselves, and this also causes the associated atmospheric rivers to be deformed [60]. After traveling to the quasi-stationary zones marked by the QSARs, waves become stationary, continue growing, and finally break. This is verified by the Hovmöller diagram (Fig. 3.1) of local wave activity (LWA), which quantifies wave breaking as a measure of zonal anomalies of potential vorticity at 250mb (see details in [57]). Although LWA is widely distributed, an enhanced area of LWA occurs on the downstream side of the QSARs, consistent with them being preferred locations of wave breaking.

We speculate the zonally and seasonally decaying Pacific jet stream, which decreases from west to east along 30°N, generates the QSAR. The decrease in jet speed probably comes from the zonally-varying meridional temperature gradient in the Pacific/Atlantic; weaker meridional temperature gradients in the Eastern Pacific/Atlantic cause the zonal jet to weaken. Additionally, the Pacific/Atlantic jet stream evolves seasonally, from being strong and extended into the Eastern Pacific/Atlantic in winter to being weak, contracted, and further north in summer. The jet carries westerly synoptic waves forming from the most unstable region downstream of the Tibetan Plateau and Rocky Mountains. These westerly waves encounter decreasing winds as they propagate downstream, becoming stationary when the background jet speed equals the phase speed of the waves, which causes them to then break [58]. As the Pacific jet weakens and contracts in summer, westerly waves break closer to East Asia/North America, and this causes the QSAR to move closer to the coast. During El Niño(La Niña) periods, the warming(cooling) east Pacific strengthens(weakens) the east Pacific jet, and consequently pushes the QSAR further east(west) during winter as observed

in Fig. 2.10a/b. Hence, El Niño(La Niña) QSARs travel longer(shorter) distances, and these probably cause different slopes of linear regressions as shown in Fig. 2.10c/d. However, this speculation still requires further theoretical support to explain the presence of the linear relationship between 40-mm exceedance date and dateline crossing date.

3.2 The QSAR recipe: Aquaplanet model simulations

In this section, we explore minimal ingredients that generate QSARs by employing a series of simplified aquaplanet model simulations. These are performed using an idealized, moist GCM [1, 82] at T42 horizontal resolution and with 25 pressure levels. To mimic the seasonal cycle, we allow the insolation to vary with time and set the shallow mixed layer depth equal to $150m$. The model surface is otherwise horizontally uniform, with a constant albedo of 0.31 and no topography. We run three cases with the following surface forcing perturbations: (1) an "aqua-Tibet" case with a $1000m$-tall Gaussian mountain located between 87.5°E–112.5°E, 10°N–50°N; (2) a tropical "warm pool–cold tongue" case with an oceanic heat flux input of $300W/m^2$ at 90°E–180°E, 15°S–15°N and -$300W/m^2$ at 180°E–90°W, 15°S–15°N; and (3) a case with both the Gaussian mountain and ocean heat fluxes. The results are presented in Fig. 3.2. The configuration of the ocean heat fluxes is intended to mimic the tropical ocean circulation given its strong influence on subtropics.

Fig. 3.2a shows Hovmöller diagrams of CWV for each of the three aquaplanet model simulations. Vertical white patches are present in cases (1) and (3) in the location of the added Gaussian mountain, consistent with the effects of topography seen in reanalysis. Localized westerly waves are also present in cases (1) and (3) to the east of the mountain. Water vapor QSARs, however, only emerge in cases (2) and (3) with ocean heat fluxes applied to the tropics. Case (3) is the only simulation with both a QSAR and westerly waves localized between the mountain and the QSAR. To summarize, the "aqua-Tibet" is necessary to localize westerly waves between the elevated topography and the QSAR, while the tropical "warm pool–cold tongue" is required to localize the QSAR.

To further diagnose the origin of westerly waves, we calculate vertically integrated tran-
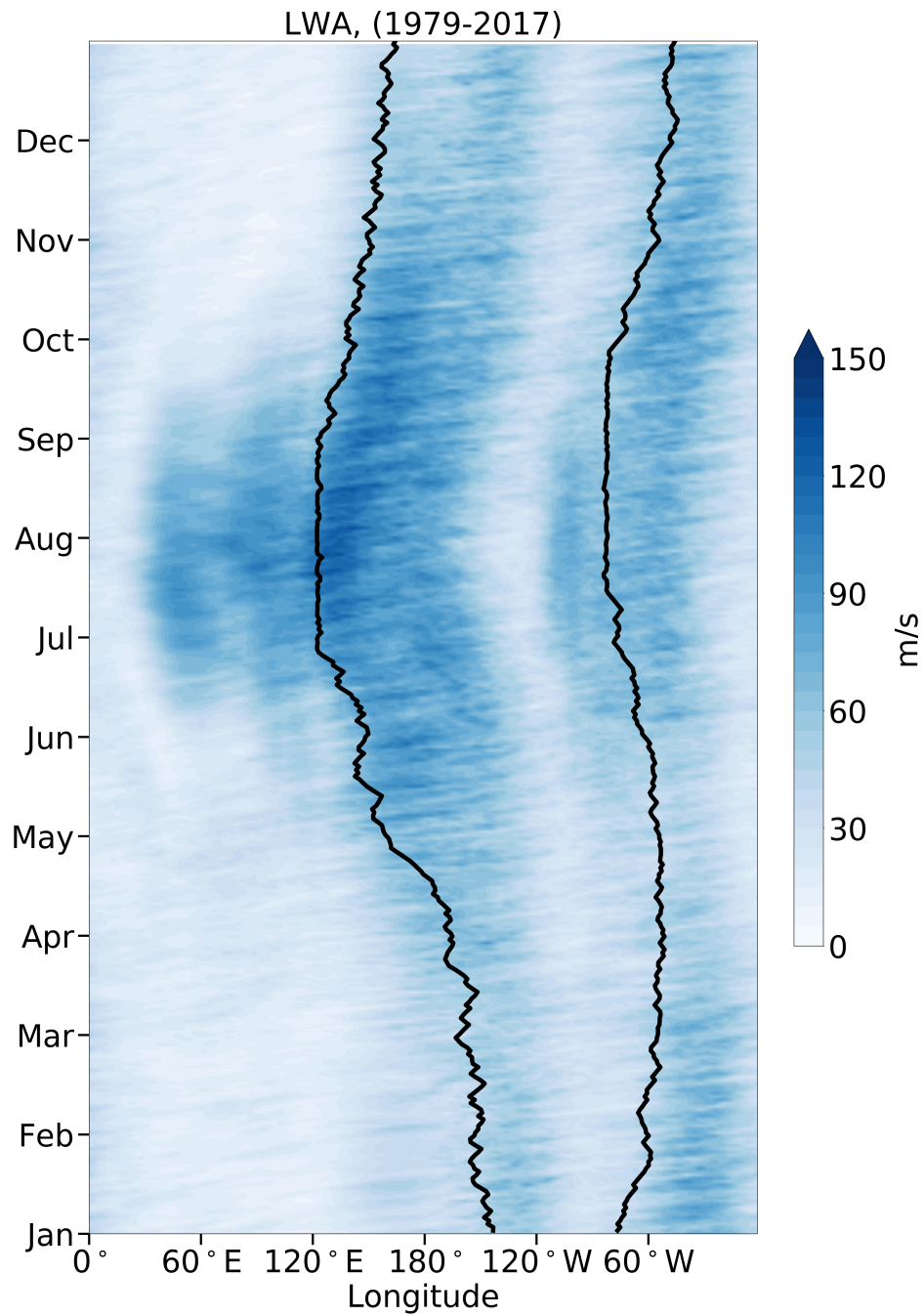
Figure 3.1: The Hovmöller diagram of daily mean climatology LWA, a measure of the non-linearity of waves, at 30°N with the addition of QSAR pathways (black curves).

sient eddy kinetic energy (EKE) defined as $\frac{1}{2}\int(u'^2+v'^2)\frac{dp}{g}$, where u' and v' are time-varying zonal and meridional wind anomalies relative to the monthly mean, p is the pressure level and g is gravitational acceleration. The strong transient EKE (Fig. 3.2b) during wintertime (DJF) in mid-latitudes shows the westerly waves seen in water vapor are the southern edges of baroclinic storms in the so-called "storm track" [83, 84, e.g.] to the leeward side of the topography. Also, the mid-latitude transient EKE directly northeast of the Gaussian mountain in cases (1) and (3) are relatively smaller than at other longitudes, implying that topography stabilizes and weakens baroclinic eddies.

3.3   The QSAR mechanism and semi-empirical model predictions

We conclude by illustrating the processes that lead to QSAR formation. The schematics in Fig. 3.3a/3.3b represent snapshots of the Pacific basin in time during the winter and summer, respectively, while Fig. 3.4/3.1 are Hovmöller diagrams of winds and local wave activity, a measure of nonlinear Rossby wave breaking. We draw inspiration from [60], who unambiguously identify atmospheric rivers with Rossby wave breaking, and as can be seen in Fig. 2.1b. The story begins with the zonally and seasonally varying Pacific jet stream, which in reanalysis data decreases from west to east along 30°N (Fig. 3.4). The decrease comes from the zonally-varying meridional temperature gradient in the Pacific; weaker meridional temperature gradients in the Eastern Pacific cause the zonal jet to weaken. The "warm pool–cold tongue" aqua-planet model simulations (Fig. 3.2b) demonstrate that the decrease of westerly wind can be found at 30°N and 180° - 120°W even though the ocean heat flow is applied along the equator.

Additionally, the Pacific jet stream evolves seasonally, from being strong and extended into the Eastern Pacific in winter to being weak and contracted in summer. The jet carries westerly waves forming from the most unstable (baroclinic) region over East Asia. We speculate that these westerly waves encounter decreasing winds as they propagate downstream, becoming stationary when the background jet speed equals the phase speed of the waves, which causes them to then break [58]. As the Pacific jet weakens and contracts in summer,
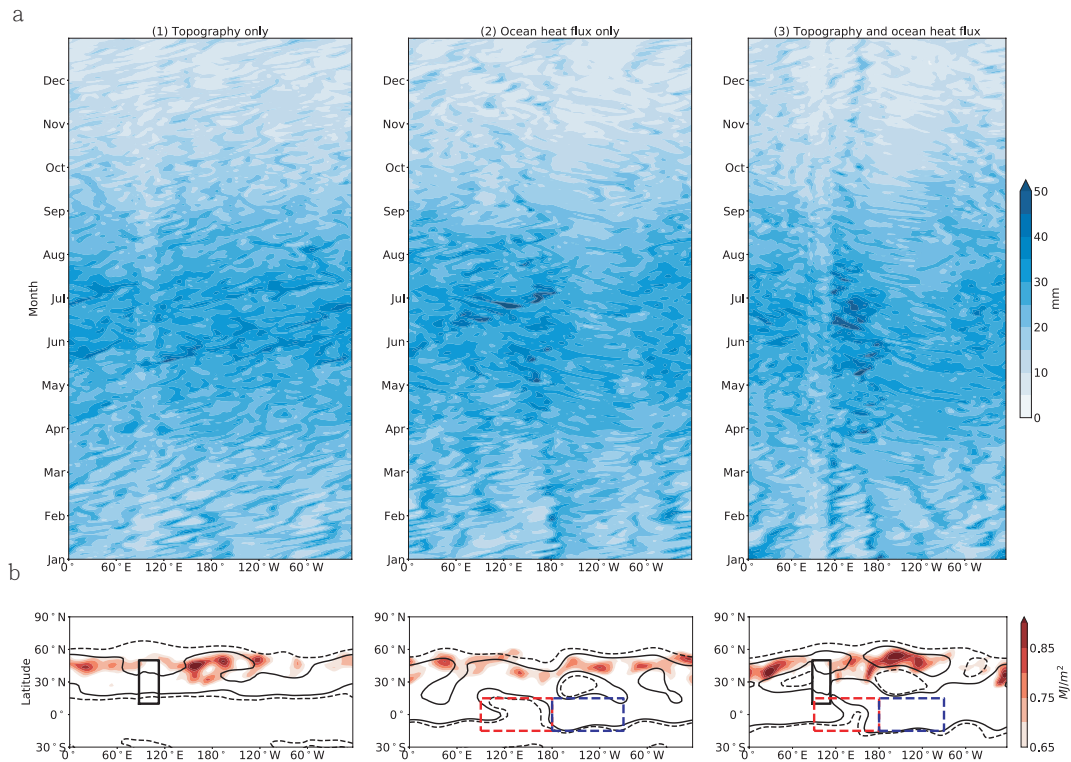
Figure 3.2: **a**. Hovmöller diagrams of CWV from three aqua-planet model simulations. **b**. Simulated wintertime (DJF) transient EKE (the red contours) and zonal wind at 250mb ($15m/s$ for the dashed black curves and $23m/s$ for the black curves). The black rectangle represents the Gaussian mountain, the red dashed rectangle is ocean heat flux output of 300 W/m^2 to the atmosphere, and the blue dashed rectangle is ocean heat flux export of -300 W/m^2.
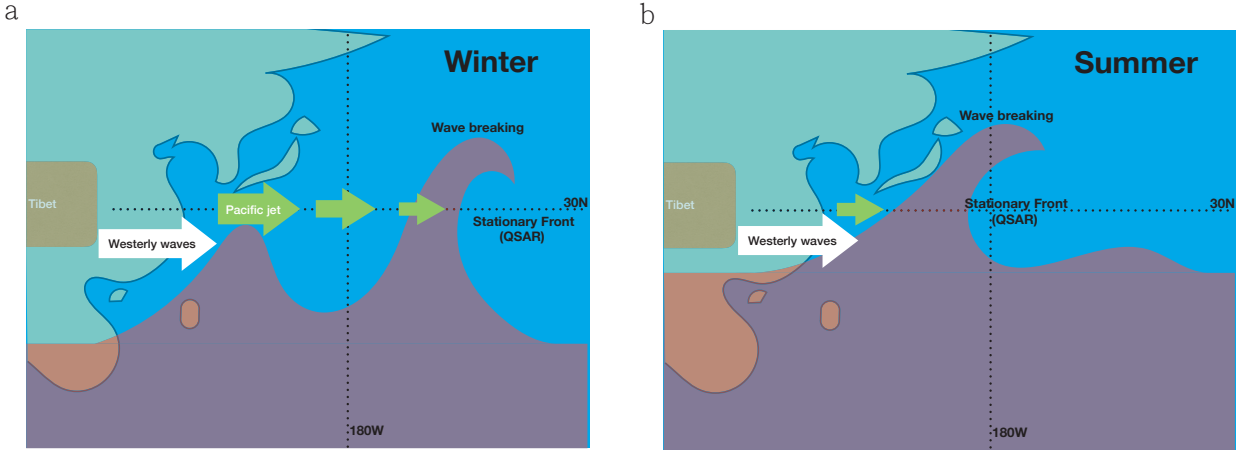
Figure 3.3: **a**. Schematic illustration of the Pacific QSAR formation during wintertime. Westerly, baroclinic waves form over East Asia (represented by white arrow), propagate downstream in the jet (green arrows) over the Pacific, and break at the location of the QSAR. Waves form local enhancements in water vapor in the subtropics (purple). **b**. Same as **a**., but during summertime.

westerly waves break closer to Asia, and this causes the QSAR to move closer to the coast.

To test our idea of wave breaking forming the QSAR, we apply two classical, analytical models of baroclinic instability: Eady's model [3] and the 2-layer quasi- geostrophic (QG) model [4]. In these models, the most unstable (wave) mode has an analytically determined phase speed [85]. This sets the condition for the wave to break downstream, where the zonal wind first decreases to match the wave's speed. We assume the maximum jet speed determines the most unstable mode, which has a typical (westward) phase speed of around 20 m/s in the Western Pacific. The mode propagates downstream until the background winds equal its phase speed; we assume this marks the location of wave breaking and QSAR formation. Both model-predicted QSAR locations agree well with the location of the CWV QSAR (Fig. 3.4). The success of such simple models, using two, distinct analytical approaches, lends credence to our theory of the seasonal migrations of a stationary wave breaking front. The baroclinic models fail during summer (Jul.-Oct.) because our assumption of spatial separation between the baroclinic zone and the wave breaking front is violated. Nevertheless, a consistent interpretation is that baroclinic modes are breaking in-place over East Asia during
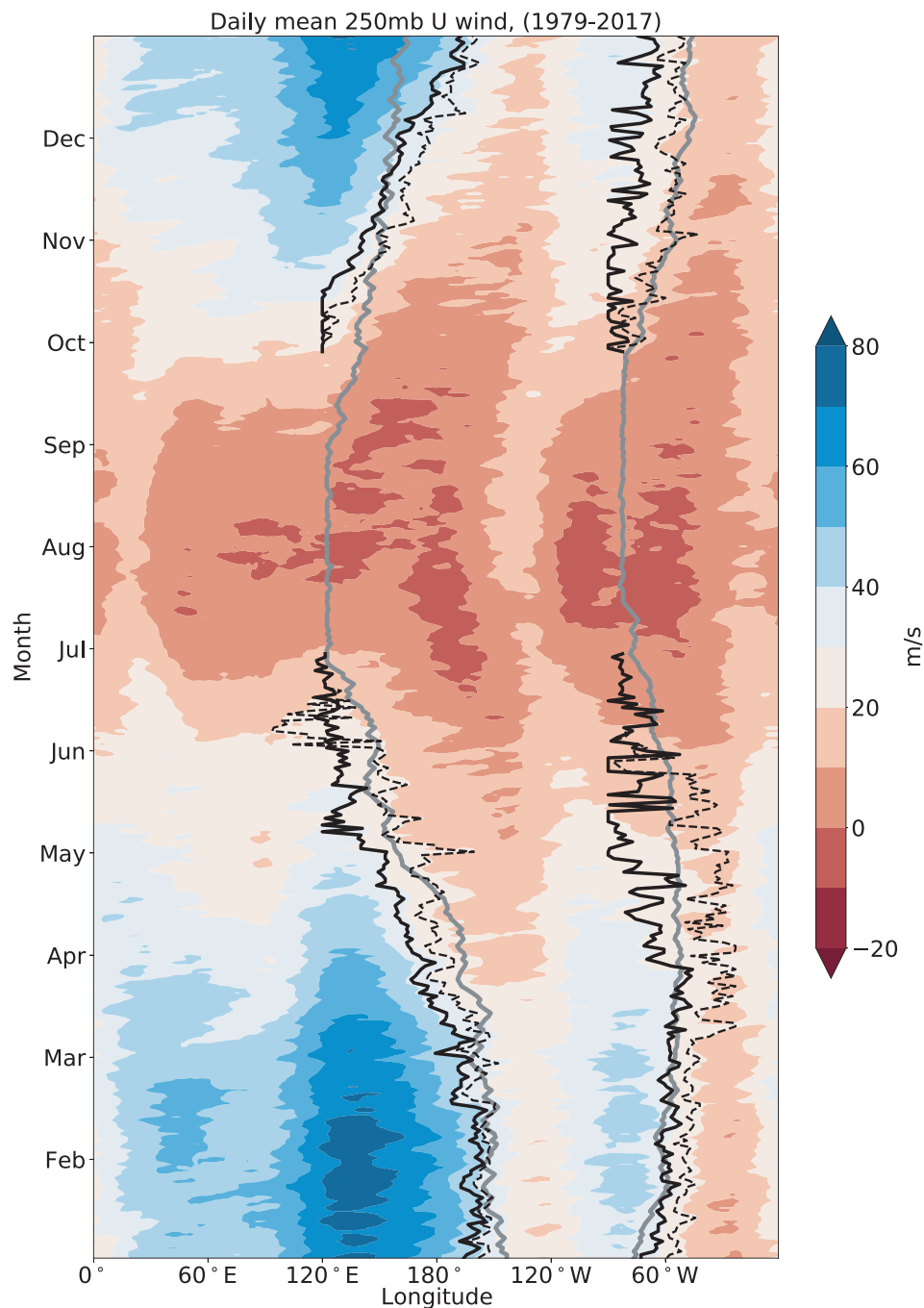
Figure 3.4: The Hovmöller diagram of ERA-Interim reanalysis of 39-year (1979-2017) climatology 250mb zonal wind at 30°N (shading) with the addition of QSAR pathways calculated from section 2.1.1 (grey curves), the predicted QSAR pathway using Eady's model (dashed black curves) and the predicted QSAR pathway using the 2-layer QG model (thick black curves).

the summer monsoon.

Westerly waves are quasi-linear at first but grow in amplitude as they propagate, eventually breaking and decaying. The typical lifecycle of a baroclinic wave is 8 days [58]. Waves keep growing during this time until reaching the stationary front (QSAR) where they break. This is verified by the Hovmöller diagram of LWA (Fig. 3.1). Although LWA is widely distributed, an enhanced area of LWA occurs on the downstream side of the QSARs, consistent with it being a preferred location of wave breaking.

In support of the linkage between QSAR and EASM, the locally enhanced low-level (850mb) wind convergence and moist static energy (MSE) roughly follow QSAR pathways (Fig. 3.5a/3.5b). The enhancement of local MSE at the QSAR is the result of humid low-level air delivered from the deep tropics by atmospheric rivers (Fig. 2.1). It decreases the gross moist stability, and could possibly trigger monsoon onset [86, 32]. A reverse argument that EASM generates the QSAR seems to be less plausible given that the chronological order of the QSAR preceeds the EASM.

3.4 Semi-empirical analytical model-predicted QSARs

The determination of model-predicted QSARs consists of three steps: (1) find the location with maximum baroclinicity, (2) numerically estimate the phase speed of the most unstable mode w.r.t. the max baroclinicity found in (1), and (3) mark the location where the jet speed matches the magnitude of the phase speed found in (2).

The first step is motivated by the expectation that maximum baroclinicity initiates the most unstable mode, which dominates over other modes in the basin [85]. We assume the major contribution causing zonally varying baroclinicity is the changing upper level (250mb) west-to-east jet stream, given the tiny zonal variations of deformation radius, surface topography and low-level jets. We also assume eddies from the Atlantic do not effect the Pacific and vice versa, so that the baroclinic maximum for each basin can be simply determined as the maximum 250mb jets over the basin itself.
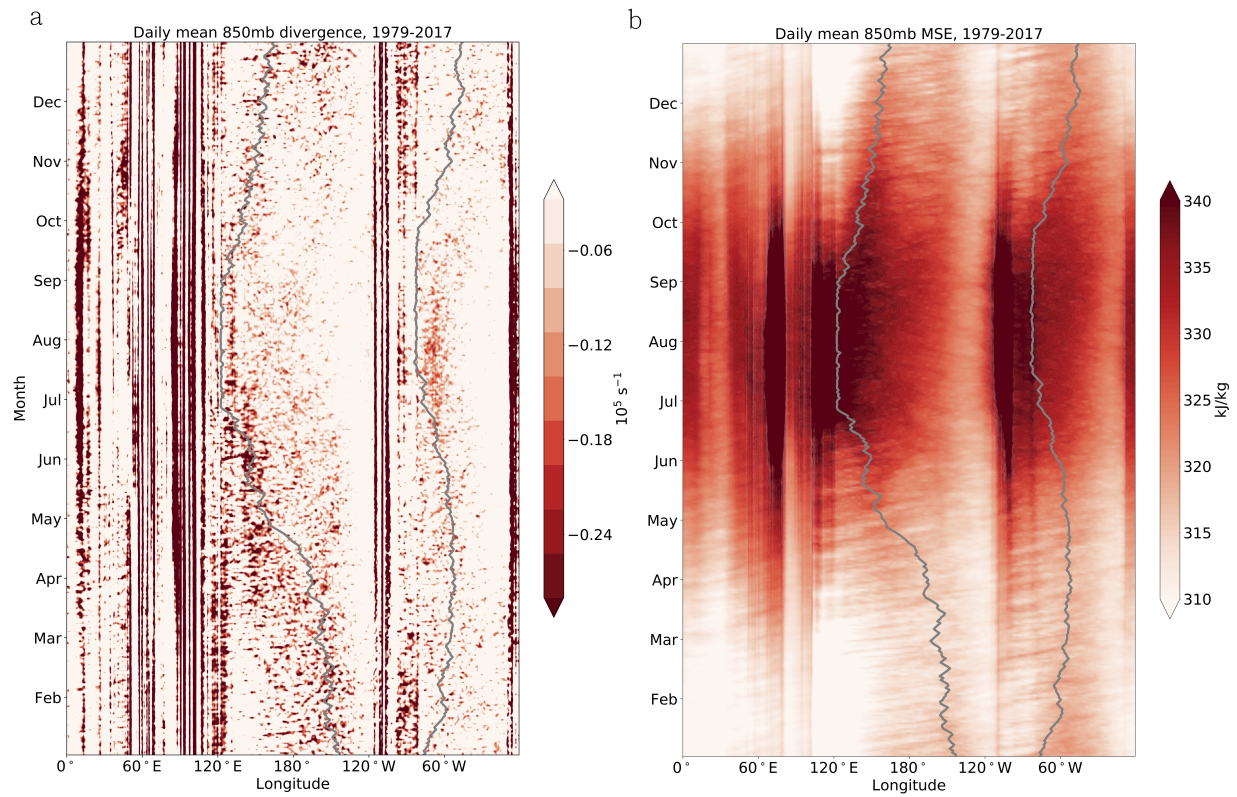
Figure 3.5: **a**. The Hovmöller diagram of daily mean climatology 850mb wind divergence at 30°N with the addition of QSAR pathways (grey curves). **b**. Same as **a**, but for 850mb MSE.

The growth rates of baroclinic waves can be determined using conventional dispersion relations of Eady and 2-layer QG models given the maximum jet speed that occurs in east Asia and north America. The maximum jet speed can be well-defined since subtropical jets and eddy-driven jets overlap in east Asia and north America [87]. Then, we numerically determine the wavenumbers of the most unstable mode with the strongest growth rates. Then the phase speeds can be obtained from the real parts of the dispersion relations. Fig. 3.6 provides the relation between maximum jet speed and the phase speed of the most unstable mode.

The last step is to find the location where the jet speed equals the phase speed. The physically meaningful locations are downstream of the jet maximum, and the distance that the baroclinic waves can reach before breaking. Although the model-predicted pathways match the QSARs locations, fluctuations of the model-predicted QSARs in Fig. 3.1 are still visible due to wind fluctuations.

We now describe the equations for Fig. 3.6. For Eady's model, the dispersion (Eq. 1.19) with flat slopes of topography and isentropes, which we assume to be small, is

$$c = \frac{U}{2}, \tag{3.1}$$

where c is a phase speed and U stands for a maximum jet stream.

For two-layer QG model, we assume baroclinic waves to be plane wave in zonal directions. The wave number with maximum growth rate is numerically defined by the imaginary part of the dispersion relation (Eq. 1.22)

$$c_i = \frac{\beta}{k^2 + k_d^2} \frac{k_d^2}{2k^2} Im \left[1 + \frac{4k^4(k^4 - k_d^4)}{k_\beta^4 k_d^4} \right]^{\frac{1}{2}}, \tag{3.2}$$

where k is the wave number, β is the Rossby parameter at the beta plane approximation, k_β is $(\beta/U)^{\frac{1}{2}}$, $k_d = 2.82/L_d$, and L_d is the deformation radius. L_d is determined by $\sqrt{gH}/f$ where $H \simeq 1.0 \times 10^4 m$ is the scale height, $g = 9.8 m/s^2$ is a gravitational acceleration, f is the coriolis parameter, and we approximate L_d to be constant in this study.

After wave number with maximum growth rate k is identified, the phase speed c_r can be
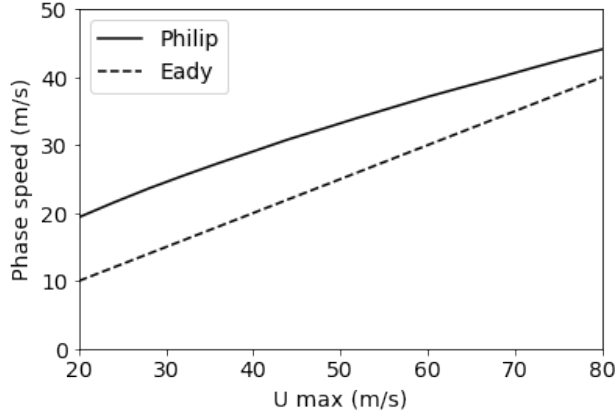
Figure 3.6: The phase speed of the most unstable mode w.r.t. the maximum speed of the jet using Eady's model (the dash line) and 2-layer QG model (the solid line).

determined by the real part of the dispersion relation

$$c_r = \frac{\beta}{k^2 + k_d^2}(1 + \frac{k_d^2}{2k^2}).$$

(3.3)

3.5 Summary

A Hovmöller diagram of 39-year climatological LWA shows that significant LWA occurs down-stream of Pacific/Atlantic QSARs, and this fact indicates that QSARs divide Pacific/Atlantic basins into linear Rossby wave and Rossby wave breaking regimes. Simplified GCM simulations [1] reveal that a Pacific-like QSAR could be simulated by inserting ocean heat fluxes similar to Pacific warm-pool/cold tongue and an aqua Tibet. A possible mechanism that can explain the emergence of QSARs is as the Pacific jet stream evolves seasonally, from being strong and extended in winter to weak and contracted in summer, Rossby waves form from baroclinic instability in East Asia and break when the most unstable mode phase speed equals the jet stream speed. As the Pacific jet weakens and contracts in summer, waves break closer to Asia, and the QSAR moves closer to the coast. This model is verified since QSAR pathways can be predicted using Eady and 2-layer QG models.

CHAPTER 4

The response of North American precipitation and temperature during LGM due to stationary waves in PMIP3 simulations

In this chapter, we switch to study the climate change effect on precipitation in North America and using LGM climate for our test case. Moistening of the American Southwest during Last Glacial Maximum (LGM, 21ka) has been identified through paleo-proxy reconstructions and tested with climate model simulations. However, the primary mechanisms driving the moistening trend are still under debate, and relatively less work has been done to study synoptic changes of precipitation in summertime. Here, by analyzing the PMIP3 simulations, we suggest that the summertime stationary waves with NW-SE tilting and eastward phase-shifting in LGM enhance precipitation in the American southwest and also dry the American southeast. LMDZ simulations indicate that Laurentide ice topography induces NW-SE tilting and ice thermodynamic effect triggers eastward phase-shifting of stationary waves. By comparing a synthesis of LGM pollen proxies to the PMIP3 ensemble, we find models that simulate a weaker Laurentide ice thermodynamic effect, weaker stationary waves with greater NW-SE tilting, and weaker jet stream anomalies compare more favorably to the proxies.

For LGM precipitation proxies, a pollen reconstruction is used that measures the precipitation anomalies between LGM and PI, and includes 29 sites over North America (see Fig. 4.1a). The precipitation proxies are obtained in many ways, for example, by categorizing pollen into different species with their characteristic climate conditions, or by calculating the biochemical production from pollen to determine climate conditions. Then, the pollen

precipitation proxies are synthesised into a North American reconstruction. A significance test is performed by comparing modern pollen reconstructed climate data with historical climate data [10, 88].

4.1 North American precipitation change and PMIP3 contraints using pollen proxies

In this section, we study precipitation change patterns that are observed in the pollen reconstructed proxies, and analyze PMIP3 model simulations to identify the governing mechanism that generates LGM precipitation change patterns in North America since PMIP3 model simulations provide the full physical state of the atmosphere during LGM. PMIP3 model-proxy data comparison is applied to divide PMIP3 model into two groups that compare favorably/unfavorably to proxies.

4.1.1 North American precipitation change during LGM forms a "dipole" pattern

Fig. 4.1a displays the annual mean precipitation anomalies of PMIP3 model ensemble average and pollen reconstruction of LGM minus PI (δP, δ stands for LGM minus PI and precipitation abbreviates to P). The contour pattern of PMIP3 model data shows a wetting southwest and a drying southeast of North America; we refer to this pattern as a "dipole". A significance test is applied to each grid by identifying whether the magnitude of δP can be differentiated from the standard deviation of PMIP3 model predictions. If the magnitude is greater than twice the standard deviation, it is significant. The result (Fig. 4.1a) indicates the dipole, with significant wetting in the southwest and drying in the southeast, is robust. A clear wetting trend is also shown in California and the Great Basin although it is not statistically significant.

We divide δP into summer (Fig. 4.1b) and winter (Fig. 4.1c) averages, chosen to represent different synoptic precipitation patterns of each season. The distinct configurations
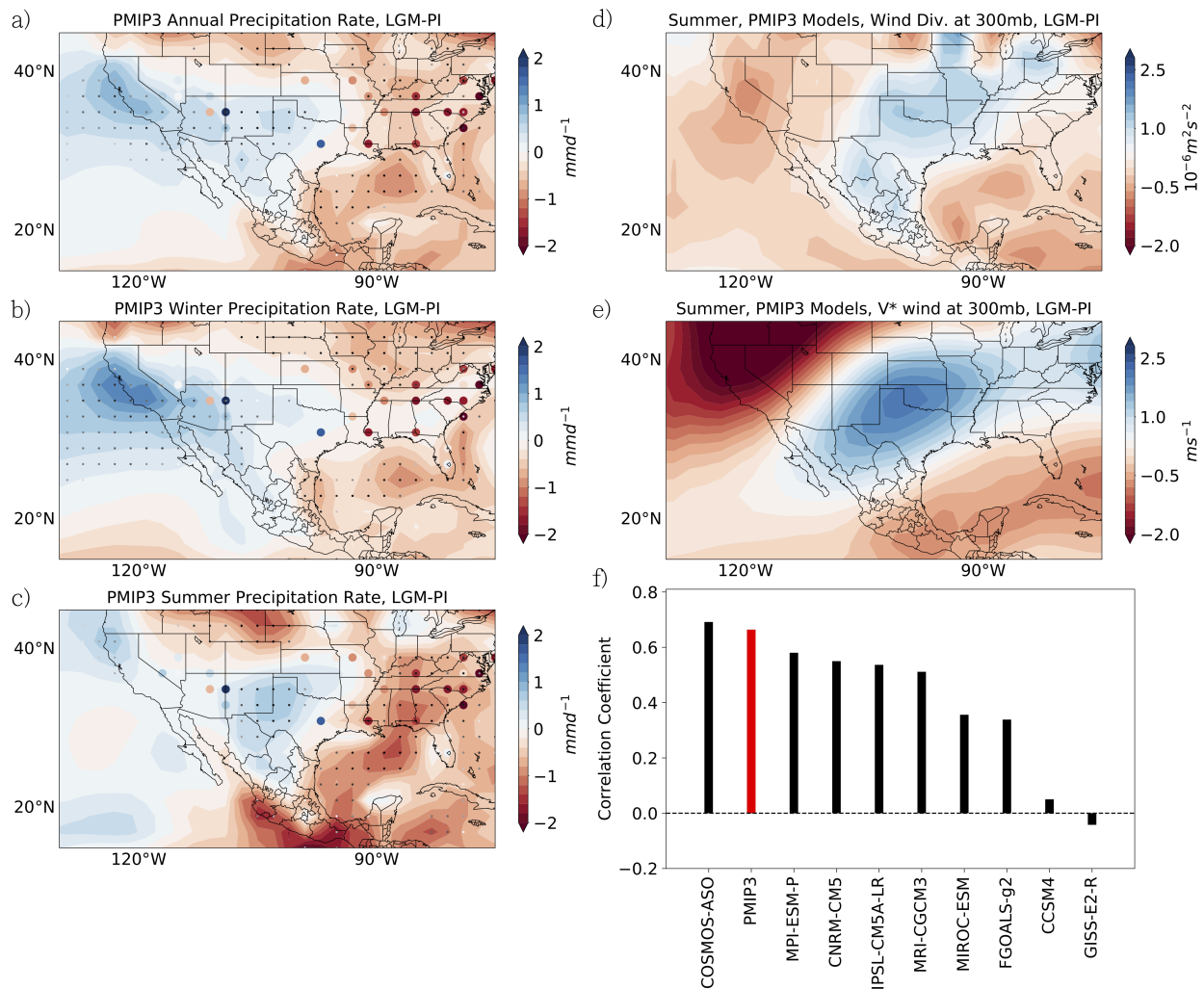
Figure 4.1: **a**. Annual mean PMIP3 ensemble mean LGM minus PI precipitation (Colored contour), pollen reconstructed data of precipitation anomaly (Colored dot), and significant change of precipitation (Black dot). **b**. Same as **a**., but for summer (MJJAS). **c**. Same as **a**, but for winter (ONDJFMA). **d**. LGM minus PI wind divergence at 300mb for summer. **e**. LGM minus PI meridional wind anomalies (v*) at 300mb for summer. Positive meridional wind (v) indicates the northward transport and the anomaly (*) stands for the deviation from the zonal mean. **f**. Correlations between PMIP3 model and proxies. PMIP3 stands for the ensemble average of all PMIP3 models.

between Fig. 4.1b/c indicates the governing mechanisms also vary seasonally. The region of increased precipitation is focused in California and the western part of the Great Basin in winter while the dipole is clearer in summer. The southward displacement of winter-season atmospheric rivers has been suggested to account for moistening trends in southern California and the western Great Basin [36]. Therefore, in this paper, we now focus more on the dynamics that forms the dipole in summer.

4.1.2 The dipole is a manifestation of stationary waves

By comparing the summer δP (Fig. 4.1b) with the 300mb wind divergence anomalies (Fig. 4.1d), and the 300mb meridional wind anomalies ($\delta v*$, where $*$ denotes zonal anomalies) in Fig. 4.1e, similar dipoles can be found in central to southeast US that indicate changes in the wind patterns correspond to the precipitation dipole. The enhanced upper level (300mb) divergence over the central US implies enhanced upward transport of air and increased low-level convergence at the bottom. This enhancement in upward motion is associated with more water vapor condensation and precipitation. In contrast, the decreasing upper level divergence in the southeastern US decreases precipitation due to a decrease in upward air transport.

Meanwhile, as shown in Fig. 4.1e, the precipitation dipole could also be contributed to the increased(decreased) $\delta v*$ that deliver warm and humid (cold and dry) air southerly(northerly) over central(southeast) US. The synchronizatized patterns of upper-level wind divergence (Fig. 4.1d) and $\delta v*$ (Fig. 4.1e) show that heat and moisture input(output) by $\delta v*$ in central(southeast) US drive upward(downward) motion and lead to upper level wind divergence(convergence) [89]. This perspective is further supported by the fact that the spatial correlation between δP and $\delta v*$ equaled 0.82.

This attribution of precipitation change can be made quantitative [47] using a moisture budget analysis [26]. The method divides the response of moisture to LGM climate into thermodynamic and dynamic terms. The thermodynamic term accounts for the Clausius-Clapeyron relation that quantifies the ability of air parcels to hold moisture under changing

temperature. The dynamics term usually represents the components of moisture change under varying wind strengths or directions in different climates. The moisture budget analysis indicates that the precipitation dipole in summer mainly results from the increasing upper level divergence that converges moisture into the southwest US (see Fig. 4e in [47]), which is consistent with arguments in the previous paragraph.

To identify the source that drives $\delta v*$ in central(southeast) US, we use wave activity flux (WAF) [56] as the vector measuring magnitudes and propagations of stationary waves to trace the factors that generate the LGM stationary wave changes (see section 1.5.3 for more details). WAF vectors diverge from their source areas and converge into sinks. In Fig. 4.2a, the deep-summer (JAS) WAF vectors originating from the subtropical low in the east Pacific and Rocky Mountains propagate across the whole North American continent and decay in the Atlantic. However, during LGM (Fig. 4.2b), this teleconnection pattern in WAF crossing North America breaks up due to the overwhelming presence of Laurentide-ice-Sheet-induced stationary waves. With the PI pathway blocked, stationary waves are forced to deflect to the southeast. WAF anomalies in LGM minus PI (Fig. 4.2c) show a southwest propagation of WAF anomalies from the Laurentide ice Sheet to the southwest US. Hence, $\delta v*$ can be viewed as the part of the stationary wave motion that originates from Laurentide ice sheet.

4.1.3 PMIP3 models that simulate weak stationary waves compare more favorably to pollen proxies

PMIP3 ensemble mean generally shows the same patterns as in reconstruction proxies for most regions, except three proxy locations show opposite trends (one in Arizona and two in Florida; 4.1a). We constrain PMIP3 model predictions by calculating correlation coefficients between the proxies and the model data at the same location as the proxies (Fig.4.1f). The PMIP3 ensemble mean preforms more favorably with the proxies than most of the individual models. To further investigate, we classify PMIP3 models into two groups. A "favorable" group contains 5 models that compare well with proxies (correlation coefficients more than 0.5) and the other one consists of the remaining 4 models (less than 0.5).

Fig. 4.3 summarizes the average of the favorable/unfavorable PMIP3 group of δP and $\delta v*$. Both groups of models simulate stationary waves with NW-SE tilting and δP dipoles that are highly correlated with their $\delta v*$. However, the favorable models are those with a weak stationary wave response during LGM. Also, the enhanced δP in the favorable PMIP3 ensemble mean occurs west of that in the unfavorable PMIP3 ensemble mean, and we suspect this can be attributed to shifts of stationary wave phases between PMIP3 models. In the next section, we discuss the mechanism that causes the δP dipole, and provide its implications for PMIP3 model constraints.

4.2 Mechanisms of the precipitation dipole and their implications for PMIP3 simulations

In this section, we perform mechanism denial experiment using the Laboratoire de Météorologie Dynamique Zoom (LMDZ) GCM, the atmospheric part of Institut Pierre-Simon Laplace (IPSL climate model) to identify the mechanisms that causes the precipitation dipole. The mechanism denial experiment relies on comparing simulations of the LMDZ with the full Laurentide ice sheet, the flat Laurentide ice, and no Laurentide ice. Hence, we can gain physical insight into the dynamics of the precipitation dipole.

4.2.1 The precipitation dipole is driven by the thermodynamics effect of the Laurentide ice sheet and NW-SE tilting is induced by Laurentide ice topography

To qualitatively investigate the primary driver of the δP dipole with NW-SE tilting, we perform a set of simulations using the LMDZ. Specifically, we analyze $v*$ using LMDZ simulations of three cases: [1] with a full Laurentide ice sheet component (Fig. 4.4a), [2] with a flat Laurentide ice sheet (Fig. 4.4b), and [3] with no ice sheet (Fig. 4.4c). We then analyze three cases of $v*$ anomalies: [1] minus [3] (Fig. 4.4d), which represents the full effect of Laurentide ice, [1] minus [2] (Fig. 4.4e), which isolates the effect of Laurentide
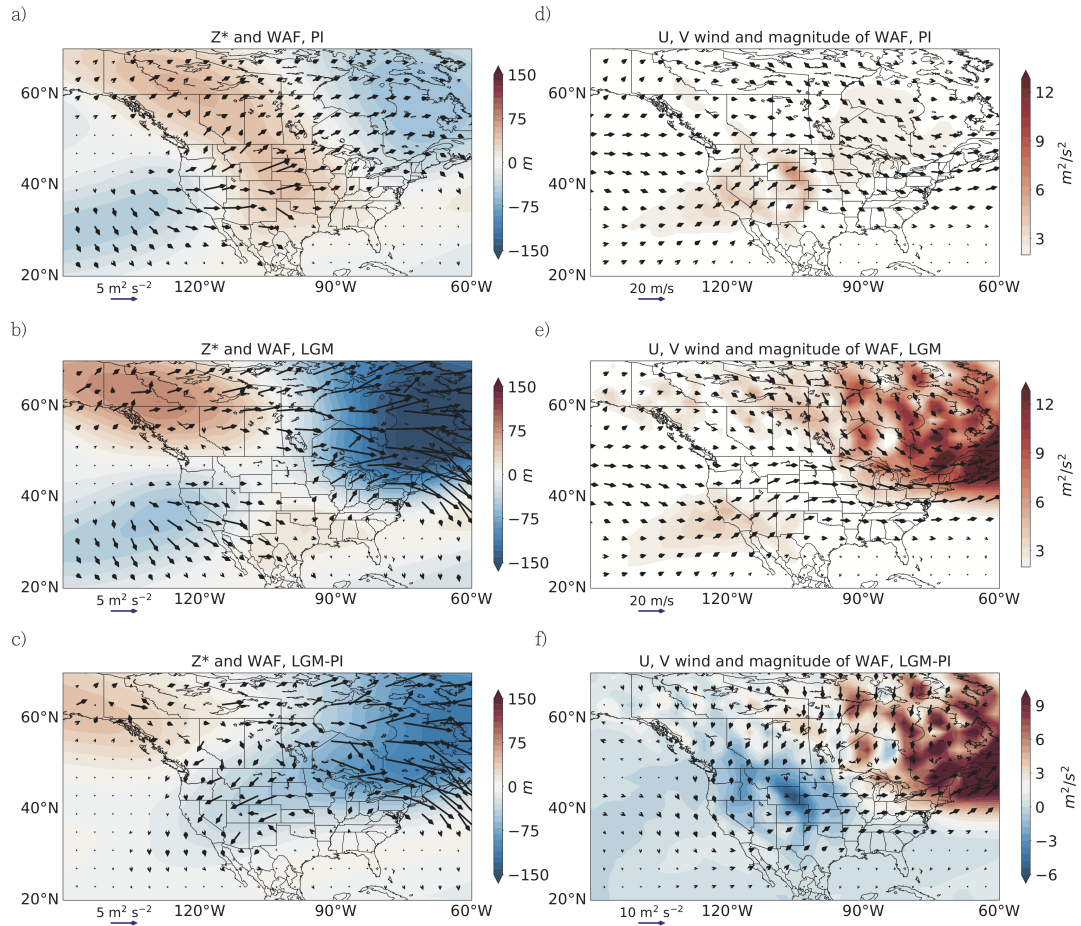
Figure 4.2: **a**. PI control run PMIP3 wave activity flux (WAF, black arrows) and geopotential height anomalies (Z*, colorful contours) at 300mb in deep summer (JAS). **b**. Same as **a**. but for LGM. **c**. Same as **a**., but for LGM-PI. **d**. PI control run PMIP3 magnitude of WAF (red contours), zonal (U) and meridional (V) winds (black arrows) at 300mb in deep summer. The magnitude of the U wind is divided by two in order to better clarify the wind vectors. **e**. Same as **d**., but for LGM. **f**. Same as **d**., but for LGM-PI.
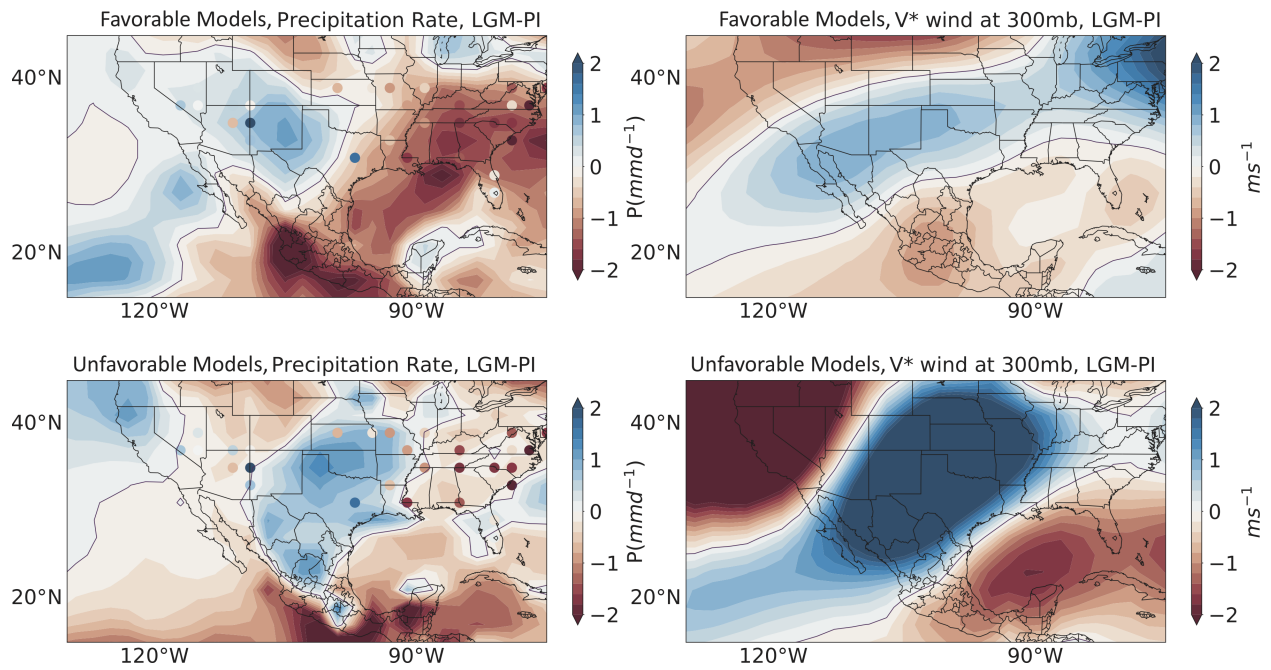
Figure 4.3: (Upper panel) Precipitation anomalies (Left) and meridional wind anomalies ($v*$) for models favorable to the proxies. (Bottem panel) The same, but for models unfavorable to the proxies.

ice topography, and [2] - [3] (Fig. 4.4f), which gives Laurentide ice thermodynamics. The dipole pattern, which consists of positive(negative) $v*$ anomalies in central(southeast) US, is apparent in Fig. 4.4d, which indicates that the dipole pattern is generated by LMDZ simulations with full effect of the Laurentide ice sheet producing a NW-SE propagating stationary wave. This gives us confidence that the LMDZ simulations can indeed help us to identify the key mechanisms behind the dipole formation.

Since the dipole phases in Fig. 4.4d compare better to the proxies than the ones in Fig. 4.4f rather than the ones in Fig. 4.4e, the formation of precipitation dipoles could be attributed to the influence of Laurentide ice thermodynamics. However, the NW-SE tilting is more likely due to the effect of Laurentide ice topography given the fact that the stationary waves in Fig. 4.4e follow NW-SE tilting while the ones in Fig. 4.4f propagate zonally. Hence, we decompose the features of the dipole into the Laurentide ice thermodynamic effect, which generates the dipole, and Laurentide ice topography effect, which tilts the dipole in NW-SE direction. The southerly wind near the US west coast from the LMDZ simulations with no Laurentide ice sheet (Fig. 4.4c) shifts to the Four Corners region with the thermodynamics effect of the Laurentide ice sheet (Fig. 4.4b). The southerly wind stays at the Four Corners region from the simulations with the addition of Laurentide ice topography (Fig. 4.4a), and this fact indicates that the dipole is generated due to phase shift and the phase shift of stationary waves is triggered by the thermodynamics effect of the Laurentide ice sheet instead of Laurentide ice topography.

The thermodynamic effect of the Laurentide ice sheet also contributes to the tilting of stationary waves. For the LMDZ simulation without Laurentide ice (Fig. 4.4c), the stationary wave travels slightly northward from the west coast of the US to mid-Canada. However, the stationary wave for the LMDZ simulation with Laurentide ice thermodynamics (Fig. 4.4b) remains in the US without tilting toward the north. This tilting induced by the thermodynamic effect of the Laurentide ice sheet is less significant compared to the tilting induced by Laurentide ice topography given the fact that stationary waves in Fig. 4.4f propagate zonally.

4.2.2 Stationary wave phase shifts due to the strengthening of jet streams by the thermodynamics effect of the Laurentide ice sheet

We now further delve into the mechanism that governs the stationary wave phase shift. Stationary wave amplitudes could be approximated by the average of summer $v*$ between 30°N-50°N where summer jet streams are strong enough (above 10 m/s) to generate mid-latitude stationary waves [90]. We define the phase angle of stationary waves at the location of $v*$ maximum inside the domain of the US continent (75°W-135°W), and the amounts of phase shift are the phase angle of stationary waves during LGM minus the ones during PI. We use the maximum of $v*$ because the stationary wave has large amplitude downstream of the Sierra Nevadas and the Rocky Mountains.

Fig. 4.5b indicates that the amounts of phase shifts positively correlate with the change of jet streams (δU), where U is defined as the maximum values of zonally averaged zonal wind in the northern hemisphere. We speculate that the stationary waves are generated as the jet streams flow across the Sierra Nevada and the Rocky Mountains. The stronger jet streams during LGM due to rising meridional temperature gradient from the presence of the Laurentide ice sheet advect stationary waves further eastward, and this effect causes the phase shifts. The relation between δU and phase shift has been calculated (the dashed black curve in Fig. 4.5b) based on the Charney-Eliassen model [2] that describes mid-latitude stationary waves forced by surface topography. We found a new solution to quantify the phase shift that is derived in the next section.

4.2.3 Predictions of phase shift by applying Charney-Eliassen theory

Charney-Eliassen theory predicts topographic induced atmospheric stationary waves using the vorticity equation with the additions of topographic forcing and surface drag. In the theory, vorticity decreases due to the shrinking depth of atmospheric column by surface topography, and decreases from surface drag. Hence, the vorticity equation could be expressed as Eq.4.1.

$$U\frac{\partial \zeta'}{\partial x} + \beta v' = -r\zeta' - \frac{fU}{H}\frac{\partial h_T}{\partial x} \tag{4.1}$$

where U is the zonally-mean zonal wind, ζ' is the zonal anomaly of vorticity, β represents a beta-plane approximation, v' is the zonal anomaly of meridional wind, r is surface drag, f is the Coriolis number, H is the scale height, and h_T is the surface topography. Assuming the surface topography has the form

$$h_T = Re[h_0 \exp(ikx)]\cos ly \tag{4.2}$$

where h_0 is the height of the mountain, k is the zonal wavenumber, and l is the meridional wave number. Hence, the solution of vorticity, as the laplacian of stream function (ψ', where $\zeta' = \nabla^2 \psi'$), becomes

$$\psi' = \frac{\tilde{h}}{(K^2 - K_S^2 - i\epsilon)}\exp(ikx)\cos ly \tag{4.3}$$

where $K^2 = k^2 + l^2$, $K_S^2 = \frac{\beta}{U}$, $\tilde{h} = \frac{fU}{H}$, and $\epsilon = \frac{rK^2}{Uk}$. We take the x derivative of ψ' to obtain v'. The phase shift angle ϕ can be derived by completing the square of denominator of Eq. 4.3.

$$
\begin{aligned}
v' &= \frac{\partial \psi'}{\partial x} \\
&= \tilde{h}k\frac{(K^2 - K_S^2) + i\epsilon}{(K^2 - K_S^2)^2 + \epsilon^2}\exp(ikx)\cos ly \\
&= \tilde{h}\frac{k}{\sqrt{(K^2 - K_S^2)^2 + \epsilon^2}}\exp[i(kx + \phi)]\cos ly \\
\cos\phi &= \frac{K^2 - K_S^2}{\sqrt{(K^2 - K_S^2)^2 + \epsilon^2}} \\
sin\phi &= \frac{\epsilon}{\sqrt{(K^2 - K_S^2)^2 + \epsilon^2}}
\end{aligned}
\tag{4.4}
$$

The maximum amplitude of ψ occurs when $\sigma^2 = (K^2 - K_S^2)^2 + \epsilon^2$ reaches minimum. We define $\epsilon = \tilde{\epsilon}K^2$, where $\tilde{\epsilon} = \frac{r}{Uk}$, and complete the square of σ.

$$
\begin{aligned}
\sigma^2 &= K^4 - 2K^2 K_S^2 + K_S^4 + \tilde{\epsilon}^2 K^4 \\
&= (1 + \tilde{\epsilon}^2)(K^2 - \frac{K_S^2}{1 + \tilde{\epsilon}^2})^2 - \frac{K_S^2}{1 + \tilde{\epsilon}^2} + K_S^4
\end{aligned}
\tag{4.5}
$$

Hence, the maximum amplitude of ψ occurs when

$$
K = \frac{K_S}{\sqrt{1 + \tilde{\epsilon}^2}}
\tag{4.6}
$$

Then, ϕ can be obtained by plugging this dispersion relation (Eq. 4.6) into Eq. 4.4 with a small angle approximation and set $\frac{U_{lgm}k}{r} = 1$.

$$
\begin{aligned}
\phi \sim \sin\phi &= -\frac{1}{\sqrt{1 + \tilde{\epsilon}^{-2}}} = -\frac{1}{\sqrt{1 + \frac{U^2 k^2}{r^2}}} \\
\delta\phi = \phi_{lgm} - \phi_{pi} &\sim (1 + \frac{U_{pi}^2 k^2}{r^2})^{\frac{-1}{2}} - (1 + \frac{U_{lgm}^2 k^2}{r^2})^{\frac{-1}{2}} \\
&= \frac{1}{\sqrt{2}}\{[1 - \frac{k^2}{2r^2}\delta(U^2)]^{\frac{-1}{2}} - 1\} \\
&\simeq \frac{k^2}{4\sqrt{2}r^2}\delta(U^2)
\end{aligned}
\tag{4.7}
$$

where $\delta(U)^2 = U_{lgm}^2 - U_{pi}^2$. Then, Eq. 4.6 reveals the phase shift angle w.r.t zonal wind anomalies. The predicted phase shift in Fig. 4.4(b) could be obtained by taking $k/r = 0.04$.

4.2.4   NW-SE tilting forms as jet streams cross Laurentide ice topography

We here discuss the mechanism that generates the NW-SE tiling of stationary waves in response to the Laurentide ice during LGM. The propagation of a stationary wave follows the vector of the wave group velocity, which varies in space due to the changing strengths of jet streams. Hence, by integrating the group velocity in space [91], the pathway of stationary waves could numerically be predicted. Given the theory of stationary wave propagation [91] is developed based on idealized conditions (an inviscid flow with strong background jet streams), the theory will be applied to qualitatively describe the behaviors of stationary

wave tilting in this study. The tilting of waves is equal to the ratio of meridional and zonal group velocities, which according to the theory, depends on the ratio of zonal and meridional wavenumbers (proportional to the inverse of wavelength):

$$\frac{\partial \omega / \partial l}{\partial \omega / \partial k} = \frac{l}{k} \tag{4.8}$$

$$l = \pm \sqrt{\frac{\beta}{U} - k^2} \tag{4.9}$$

As Laurentide ice forms during LGM, the ice topography induces an eastward propagating stationary wave with lower k (longer wavelength) than the Rocky Mountains. Hence, this ice topography induced stationary wave has greater l values according to Eq. 4.9 and propagates toward the southeast (for $l > 0$; the solution with $l < 0$ propagates toward the northeast and does not influence our region of interest). Stronger jet streams, U, zonalize stationary wave propagations by reducing l through lowering β/U, which leads to less tilting. Weaker U, on the contrary, induce greater meridional wave propagation by enhancing l through increasing β/U, and force stationary tilting meridionally. This fact explains the slightly northward tilting observed in Fig. 4.4c given the weaker jet streams during PI-control run.

4.3 Summary

By analyzing the pollen reconstructed precipitation proxies during LGM and comparing to PMIP3 model simulations, we find that the precipitation change during LGM forms a dipole with a wetting southwest and a drying southeast of the US. PMIP3 model simulations further show that the precipitation dipole can be mainly attributed to LGM meridional wind anomalies associated with summer stationary waves. The precipitation dipole forms as southerly wind brings warm and humid air into the southwest US while the northerly wind transports cold and dry air into the southeast US.

The WAF analysis indicates that those stationary waves are developed locally instead of remotely. By applying LMDZ simulations, we identified that the NW-SE tilting is triggered
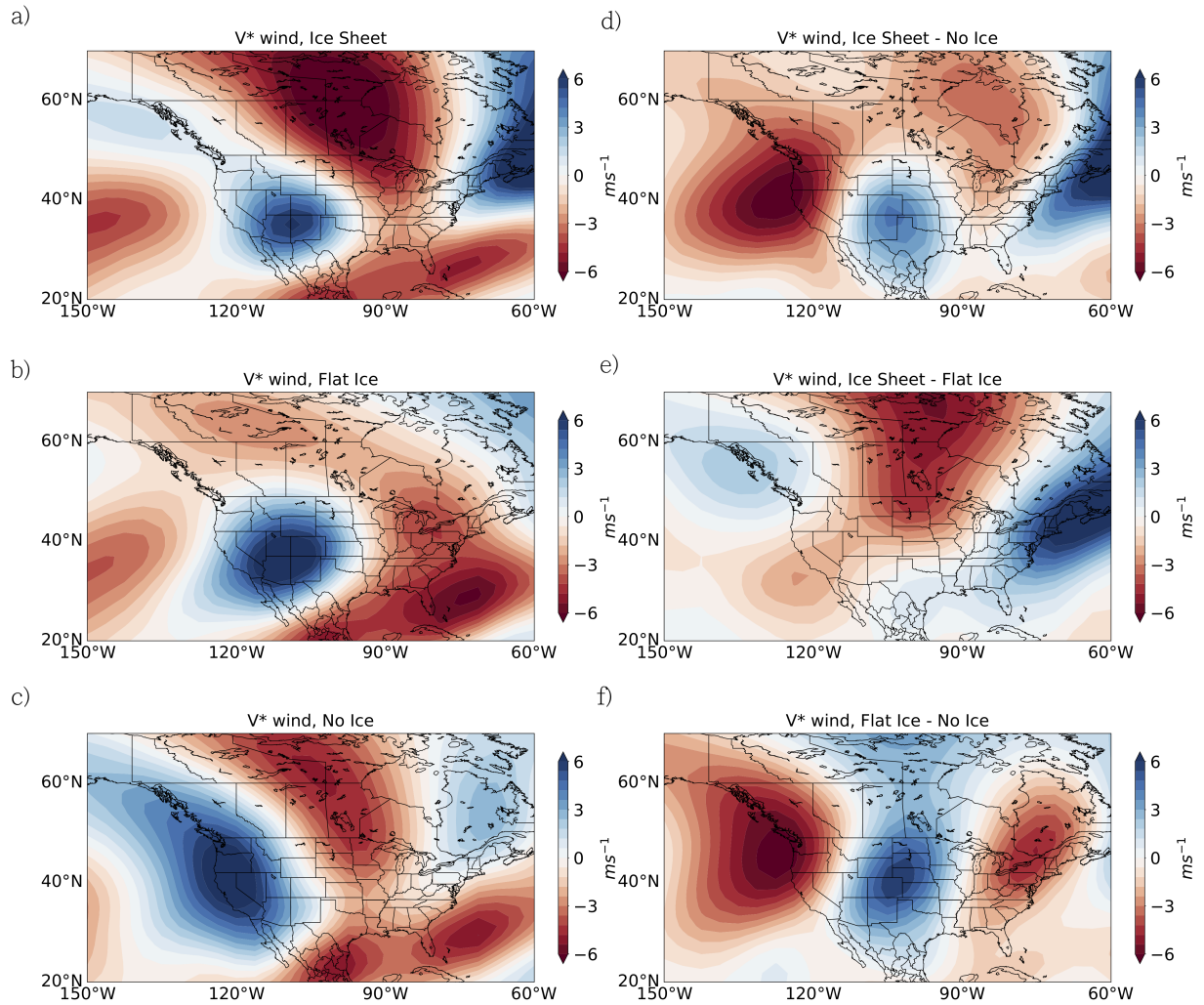
Figure 4.4: LMDZ simulations of zonal anomalies of meridional wind ($V*$) with **a**. full Laurentide ice sheet **b**. flat Laurentide ice **c**. no Laurentide ice, and $V*$ of **d**. full Laurentide ice sheet minus no Laurentide ice **e**. Laurentide ice sheet minus flat Laurentide ice **f**. flat Laurentide ice minus no Laurentide ice.
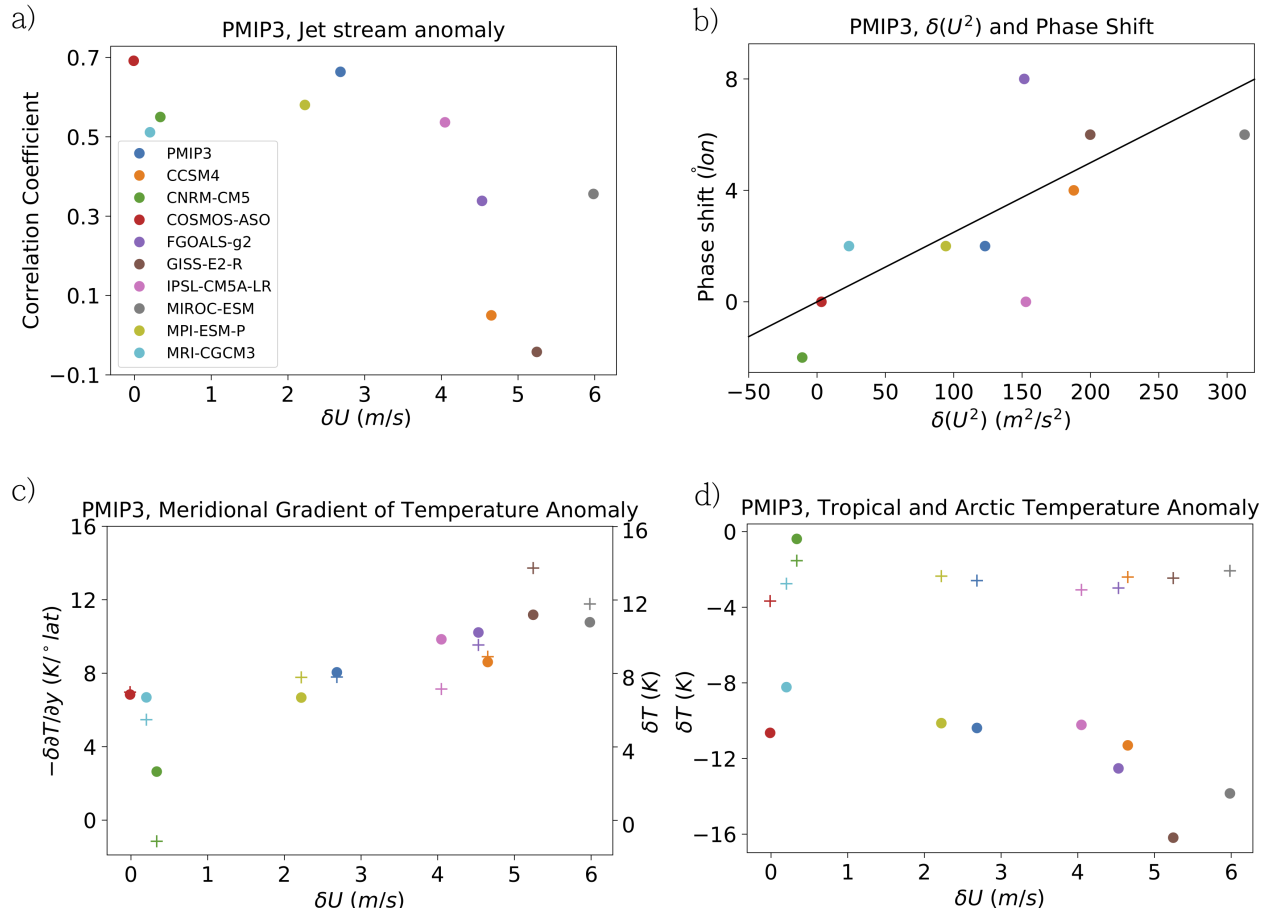
Figure 4.5: **a**. The change of the zonal mean jet stream strengths, δU, with correlation between PMIP3 model and proxies. The strength of the jet streams is determined by the latitude with the strongest jet streams. **b**. The change of stationary wave phase and δU^2. The black straight line shows predictions by Charney-Eliassen model. **c**. δU, zonal mean of changing vertically averaged meridional temperature gradient $\delta \frac{\partial \bar{T}}{\partial y}$ (marked by circles), and the changing equator-to-pole temperature difference (marked by plus signs). The meridional temperature gradient is at latitude of δU in the surface level. **d**. The change of surface temperature in the tropics (marked by plus signs) and in the Arctic (marked by circles).

by Laurentide ice topography and the thermodynamic effect of Laurentide ice causes the precipitation dipole to shift the stationary wave phases toward the east. The amounts of phase shift can be quantified by applying a new solution of the Charney-Eliassen model and positively correlate with the changing strengths of LGM jet streams.

The PMIP3 Model- pollen data constraint indicates that models with weaker jet streams and stationary wave amplitudes compare favorably to the proxies. The thermal wind balance could be further applied to quantitatively explain that the jet stream strengths positively correlate with the equator-to-pole temperature difference. Since there is a strong disagreement of PMIP3 models for LGM polar temperature, our study implies that weak polar amplification compares more favorably with the proxies.

CHAPTER 5

Conclusion

In this dissertation, we discuss the discovery of localized, quasi-stationary zones of atmospheric rivers and develop a tracking-algorithm to identify QSAR pathways. The Pacific QSAR has predictive skill for EASM onsets, specifically when the CWV of Pacific QSARs first exceeds 40mm during strong ENSO periods. We also speculate on origin of QSAR dynamics from the perspective of synoptic wave breaking. We suspect that the seasonal contractions of zonally decaying jet streams form quasi-stationary zones of atmospheric rivers (QSARs). This speculation needs to be tested by climate model simulations and quasi-geostrophic theories to explore QSAR formation mechanisms with different migrating speeds during ENSO. We plan to extend the study to a wider range of latitudes given the presence of QSAR features in 25°N-40°N, and to include an improved tracking algorithm that better identifies QSAR pathways.

The evidence for repeating QSARs in CWV Hovmöller diagrams for the past 39-years shows the climate components of synoptic atmospheric rivers. The fact that the Pacific QSAR dateline crossing date leads EASM onset implies that it could be strongly affected by the zonal and seasonal migrations of QSARs. The strong predictive skill of EASM onset during strong ENSO indicates the predictability of year-to-year variability of EASM onset, and also shows the power of a CWV-based monsoon proxy to better identify details of longitudinal-temporal structures of the EASM. This study opens a new perspective that incorporates mid-latitude wave dynamics in the description of EASM onset mechanisms instead of the more conventional mechanisms such as sea-breeze and meridional migrations of ITCZ.

We also compare a synthesis of pollen reconstructed proxies of LGM precipitation and

confirm the existence of a spatial dipole pattern in summer North American precipitation. In PMIP3 simulations of the LGM minus pre-industrial conditions, the precipitation dipole is the manifestation of the stationary wave that travels from NW to SE. By comparing LMDZ simulations with the full Laurentide ice, flat Laurentide ice and no Laurentide ice, we attribute the precipitation dipole to the shifting phases of stationary waves due to the thermodynamic effect of the Laurentide ice. The Laurentide ice topography forces the stationary waves to tilt NW-SE. By further applying vorticity equations, we conclude that stronger jet streams cause stationary waves to propagate more zonally with larger phase shifts. The thermal wind balance is also applied to qualitatively explain the fact that the strengths of the jet streams correlate positively with the equator-to-pole surface temperature difference. From PMIP3 model-proxy data comparison, the PMIP3 models that simulate weak stationary waves (smaller phase shifts), large NW-SE tilting, strong jet streams and weak summer polar amplifications compare favorably with proxies. Our study suggests that more effort should be made to improve the parameterizations of summer sea ice, and our understanding how the Laurentide ice sheet reconfigures stationary wave patterns during the LGM.

REFERENCES

[1] Dargan MW Frierson, Isaac M Held, and Pablo Zurita-Gotor. A gray-radiation aqua-planet moist gcm. part i: Static stability and eddy scale. *Journal of the Atmospheric Sciences*, 63(10):2548–2566, 2006.

[2] Jule G Charney and Arnt Eliassen. A numerical method for predicting the perturbations of the middle latitude westerlies. *Tellus*, 1(2):38–54, 1949.

[3] ERIC T Eady. Long waves and cyclone waves. *Tellus*, 1(3):33–52, 1949.

[4] Norman A Phillips. Energy transformations and meridional circulations associated with simple baroclinic waves in a two-level, quasi-geostrophic model. *Tellus*, 6(3):274–286, 1954.

[5] IPCC. *Summary for Policymakers*, book section SPM, page 1–30. Cambridge University Press, Cambridge, United Kingdom and New York, NY, USA, 2013.

[6] Bin Wang. Rainy season of the asian–pacific summer monsoon. *Journal of Climate*, 15(4):386–398, 2002.

[7] PJ Webster. The elementary monsoon. monsoons, js fein and pl stephens, eds, 1987.

[8] PJ Webster and J Fasullo. Encyclopedia of atmospheric sciences 1370–1385, 2003.

[9] Dick P Dee, SM Uppala, AJ Simmons, Paul Berrisford, P Poli, S Kobayashi, U Andrae, MA Balmaseda, G Balsamo, d P Bauer, et al. The era-interim reanalysis: Configuration and performance of the data assimilation system. *Quarterly Journal of the royal meteorological society*, 137(656):553–597, 2011.

[10] PJ Bartlein, SP Harrison, Sandra Brewer, S Connor, BAS Davis, K Gajewski, Joel Guiot, TI Harrison-Prentice, A Henderson, Odile Peyron, et al. Pollen-based continental climate reconstructions at 6 and 21 ka: a global synthesis. *Climate Dynamics*, 37(3-4):775–802, 2011.

[11] Simona Bordoni and Tapio Schneider. Regime transitions of steady and time-dependent hadley circulations: Comparison of axisymmetric and eddy-permitting simulations. *Journal of the Atmospheric Sciences*, 67(5):1643–1654, 2010.

[12] Tapio Schneider and Simona Bordoni. Eddy-mediated regime transitions in the seasonal cycle of a hadley circulation and implications for monsoon dynamics. *Journal of the Atmospheric Sciences*, 65(3):915–934, 2008.

[13] Isaac M Held and Arthur Y Hou. Nonlinear axially symmetric circulations in a nearly inviscid atmosphere. *Journal of the Atmospheric Sciences*, 37(3):515–533, 1980.

[14] Richard S Lindzen and Arthur V Hou. Hadley circulations for zonally averaged heating centered off the equator. *Journal of the Atmospheric Sciences*, 45(17):2416–2427, 1988.

[15] R Alan Plumb and Arthur Y Hou. The response of a zonally symmetric atmosphere to subtropical thermal forcing: Threshold behavior. *Journal of the atmospheric sciences*, 49(19):1790–1799, 1992.

[16] Kerry A Emanuel. On thermally direct circulations in moist atmospheres. *Journal of the atmospheric sciences*, 52(9):1529–1534, 1995.

[17] Christopher C Walker and Tapio Schneider. Eddy influences on hadley circulations: Simulations with an idealized gcm. *Journal of the atmospheric sciences*, 63(12):3333–3350, 2006.

[18] Shang-Ping Xie and Naomi Saiki. Abrupt onset and slow seasonal evolution of summer monsoon in an idealized gcm simulation. *Journal of the Meteorological Society of Japan. Ser. II*, 77(4):949–968, 1999.

[19] Nikki C Privé and R Alan Plumb. Monsoon dynamics with interactive forcing. part ii: Impact of eddies and asymmetric geometries. *Journal of the atmospheric sciences*, 64(5):1431–1442, 2007.

[20] Mark J Rodwell and Brian J Hoskins. Monsoons and the dynamics of deserts. *Quarterly Journal of the Royal Meteorological Society*, 122(534):1385–1404, 1996.

[21] William R Boos and Zhiming Kuang. Dominant control of the south asian monsoon by orographic insulation versus plateau heating. *Nature*, 463(7278):218, 2010.

[22] Spencer A Hill, Simona Bordoni, and Jonathan L Mitchell. Axisymmetric constraints on cross-equatorial hadley cell extent. *Journal of the Atmospheric Sciences*, 76(6):1547–1564, 2019.

[23] Simona Bordoni and Tapio Schneider. Monsoons as eddy-mediated regime transitions of the tropical overturning circulation. *Nature Geoscience*, 1(8):515, 2008.

[24] Isaac M Held. The gap between simulation and understanding in climate modeling. *Bulletin of the American Meteorological Society*, 86(11):1609–1614, 2005.

[25] Isaac M Held and Brian J Soden. Robust responses of the hydrological cycle to global warming. *Journal of climate*, 19(21):5686–5699, 2006.

[26] Richard Seager, David Neelin, Isla Simpson, Haibo Liu, Naomi Henderson, Tiffany Shaw, Yochanan Kushnir, Mingfang Ting, and Benjamin Cook. Dynamical and thermodynamical causes of large-scale changes in the hydrological cycle over north america in response to global warming. *Journal of Climate*, 27(20):7921–7948, 2014.

[27] Isla R Simpson, Richard Seager, Mingfang Ting, and Tiffany A Shaw. Causes of change in northern hemisphere winter meridional winds and regional hydroclimate. *Nature Climate Change*, 6(1):65, 2016.

[28] J David Neelin and Isaac M Held. Modeling tropical convergence based on the moist static energy budget. *Monthly Weather Review*, 115(1):3–12, 1987.

[29] Sarah M Kang, Isaac M Held, Dargan MW Frierson, and Ming Zhao. The response of the itcz to extratropical thermal forcing: Idealized slab-ocean experiments with a gcm. *Journal of Climate*, 21(14):3521–3532, 2008.

[30] John CH Chiang and Andrew R Friedman. Extratropical cooling, interhemispheric thermal gradients, and tropical climate change. *Annual Review of Earth and Planetary Sciences*, 40, 2012.

[31] David McGee, Aaron Donohoe, John Marshall, and David Ferreira. Changes in itcz location and cross-equatorial heat transport at the last glacial maximum, heinrich stadial 1, and the mid-holocene. *Earth and Planetary Science Letters*, 390:69–79, 2014.

[32] Anji Seth, Sara A Rauscher, Michela Biasutti, Alessandra Giannini, Suzana J Camargo, and Maisa Rojas. Cmip5 projected changes in the annual cycle of precipitation in monsoon regions. *Journal of climate*, 26(19):7328–7351, 2013.

[33] John G Dwyer, Michela Biasutti, and Adam H Sobel. The effect of greenhouse gas–induced changes in sst on the annual cycle of zonal mean tropical precipitation. *Journal of Climate*, 27(12):4544–4565, 2014.

[34] Raymond T Pierrehumbert. The hydrologic cycle in deep-time climate problems. *Nature*, 419(6903):191, 2002.

[35] Sukyoung Lee and Hyun-kyung Kim. The dynamical relationship between subtropical and eddy-driven jets. *Journal of the atmospheric sciences*, 60(12):1490–1503, 2003.

[36] Juan M Lora, Jonathan L Mitchell, Camille Risi, and Aradhna E Tripati. North pacific atmospheric rivers and their influence on western north america at the last glacial maximum. *Geophysical Research Letters*, 44(2):1051–1059, 2017.

[37] Gang Chen, Isaac M Held, and Walter A Robinson. Sensitivity of the latitude of the surface westerlies to surface friction. *Journal of the atmospheric sciences*, 64(8):2899–2915, 2007.

[38] Thomas F Stocker, Q Dahe, and Gian-Kasper Plattner. Climate change 2013: The physical science basis. *Working Group I Contribution to the Fifth Assessment Report of the Intergovernmental Panel on Climate Change. Summary for Policymakers (IPCC, 2013)*, 2013.

[39] Jeffrey S Munroe and Benjamin JC Laabs. Temporal correspondence between pluvial lake highstands in the southwestern us and heinrich event 1. *Journal of Quaternary Science*, 28(1):49–58, 2013.

[40] Daniel E Ibarra, Anne E Egger, Karrie L Weaver, Caroline R Harris, and Kate Maher. Rise and fall of late pleistocene pluvial lakes in response to reduced evaporation and precipitation: Evidence from lake surprise, california. *Bulletin*, 126(11-12):1387–1415, 2014.

[41] Jessica L Oster, Isabel P Montañez, Warren D Sharp, and Kari M Cooper. Late pleistocene california droughts during deglaciation and arctic warming. *Earth and Planetary Science Letters*, 288(3-4):434–443, 2009.

[42] Jessica L Oster, Isabel P Montanez, Laura R Santare, Warren D Sharp, Corinne Wong, and Kari M Cooper. Stalagmite records of hydroclimate in central california during termination 1. *Quaternary Science Reviews*, 127:199–214, 2015.

[43] Daniel L Swain, Daniel E Horton, Deepti Singh, and Noah S Diffenbaugh. Trends in atmospheric patterns conducive to seasonal precipitation and temperature extremes in california. *Science Advances*, 2(4):e1501344, 2016.

[44] Jessica L Oster and Neil P Kelley. Tracking regional and global teleconnections recorded by western north american speleothem records. *Quaternary Science Reviews*, 149:18–33, 2016.

[45] Cohmap Members. Climatic changes of the last 18,000 years: observations and model simulations. *Science*, pages 1043–1052, 1988.

[46] Yemane Asmerom, Victor J Polyak, and Stephen J Burns. Variable winter moisture in the southwestern united states linked to rapid glacial climate shifts. *Nature Geoscience*, 3(2):114, 2010.

[47] Juan M Lora. Components and mechanisms of hydrologic cycle changes over north america at the last glacial maximum. *Journal of Climate*, 31(17):7035–7051, 2018.

[48] Camille Li and David S Battisti. Reduced atlantic storminess during last glacial maximum: Evidence from a coupled climate model. *Journal of Climate*, 21(14):3561–3579, 2008.

[49] Marcus Löfverström, Rodrigo Caballero, Johan Nilsson, and Johan Kleman. Evolution of the large-scale atmospheric circulation in response to changing ice sheets over the last glacial cycle. *Climate of the Past*, 10(4):1453–1471, 2014.

[50] Marcus Löfverström and Juan M Lora. Abrupt regime shifts in the north atlantic atmospheric circulation over the last deglaciation. *Geophysical Research Letters*, 44(15):8047–8055, 2017.

[51] Marcus Löfverström, Rodrigo Caballero, Johan Nilsson, and Gabriele Messori. Stationary wave reflection as a mechanism for zonalizing the atlantic winter jet at the lgm. *Journal of the Atmospheric Sciences*, 73(8):3329–3342, 2016.

[52] Tripti Bhattacharya, Jessica E Tierney, Jason A Addison, and James W Murray. Icesheet modulation of deglacial north american monsoon intensification. *NATURE GEOSCIENCE*, 11(11):848–+, 2018.

[53] Tripti Bhattacharya, Jessica E Tierney, and Pedro DiNezio. Glacial reduction of the north american monsoon via surface cooling and atmospheric ventilation. *Geophysical Research Letters*, 44(10):5113–5122, 2017.

[54] Isaac M Held, Mingfang Ting, and Hailan Wang. Northern winter stationary waves: Theory and modeling. *Journal of climate*, 15(16):2125–2144, 2002.

[55] Prashant D Sardeshmukh and Brian J Hoskins. The generation of global rotational flow by steady idealized tropical divergence. *Journal of the Atmospheric Sciences*, 45(7):1228–1251, 1988.

[56] R Alan Plumb. On the three-dimensional propagation of stationary waves. *Journal of the Atmospheric Sciences*, 42(3):217–229, 1985.

[57] Clare SY Huang and Noboru Nakamura. Local finite-amplitude wave activity as a diagnostic of anomalous weather events. *Journal of the Atmospheric Sciences*, 73(1):211–229, 2016.

[58] CD Thorncroft, BJ Hoskins, and ME McIntyre. Two paradigms of baroclinic-wave life-cycle behaviour. *Quarterly Journal of the Royal Meteorological Society*, 119(509):17–55, 1993.

[59] Kerry H Cook and Isaac M Held. Stationary waves of the ice age climate. *Journal of climate*, 1(8):807–819, 1988.

[60] Ashley E Payne and Gudrun Magnusdottir. Dynamics of landfalling atmospheric rivers over the north pacific in 30 years of merra reanalysis. *Journal of Climate*, 27(18):7133–7150, 2014.

[61] Zhang Renhe. Relations of water vapor transport from indian monsoon with that over east asia and the summer rainfall in china. *Advances in Atmospheric Sciences*, 18(5):1005–1017, 2001.

[62] Suxiang Yao, Qian Huang, Yaocun Zhang, and Xu Zhou. The simulation of water vapor transport in east asia using a regional air–sea coupled model. *Journal of Geophysical Research: Atmospheres*, 118(4):1585–1600, 2013.

[63] Chen Pan, Bin Zhu, Jinhui Gao, and Hanqing Kang. Source apportionment of atmospheric water over east asia–a source tracer study in cam5. 1. *Geoscientific Model Development*, 10(2):673–688, 2017.

[64] Chiqin Li, Qunjie Zuo, Xiangde Xu, and Shouting Gao. Water vapor transport around the tibetan plateau and its effect on summer rainfall over the yangtze river valley. *Journal of Meteorological Research*, 30(4):472–482, 2016.

[65] Liu Yong and Ronghui Huang. Linkages between the south and east asian monsoon water vapor transport during boreal summer. *Journal of Climate*, (2019), 2019.

[66] Xiuzhen Li and Wen Zhou. Quasi-4-yr coupling between el niño–southern oscillation and water vapor transport over east asia–wnp. *Journal of Climate*, 25(17):5879–5891, 2012.

[67] Youichi Kamae, Wei Mei, and Shang-Ping Xie. Climatological relationship between warm season atmospheric rivers and heavy rainfall over east asia. *Journal of the Meteorological Society of Japan. Ser. II*, 2017.

[68] Youichi Kamae, Wei Mei, Shang-Ping Xie, Moeka Naoi, and Hiroaki Ueda. Atmospheric rivers over the northwestern pacific: Climatology and interannual variability. *Journal of Climate*, 30(15):5605–5619, 2017.

[69] Bryan D Mundhenk, Elizabeth A Barnes, and Eric D Maloney. All-season climatology and variability of atmospheric river frequencies over the north pacific. *Journal of Climate*, 29(13):4885–4903, 2016.

[70] Ole Peters and J David Neelin. Critical phenomena in atmospheric precipitation. *Nature physics*, 2(6):393, 2006.

[71] Renguang Wu and Bin Wang. Interannual variability of summer monsoon onset over the western north pacific and the underlying processes. *Journal of climate*, 13(14):2483–2501, 2000.

[72] Minoru Tanaka. Interannual and interdecadal variations of the western north pacific monsoon and baiu rainfall and their relationship to the enso cycles. *Journal of the Meteorological Society of Japan. Ser. II*, 75(6):1109–1123, 1997.

[73] Jianhua Ju and Julia Slingo. The asian summer monsoon and enso. *Quarterly Journal of the Royal Meteorological Society*, 121(525):1133–1168, 1995.

[74] Bo Wu, Tianjun Zhou, and Tim Li. Seasonally evolving dominant interannual variability modes of east asian climate. *Journal of Climate*, 22(11):2992–3005, 2009.

[75] Ngar-Cheung Lau and Mary Jo Nath. Atmosphere–ocean variations in the indo-pacific sector during enso episodes. *Journal of Climate*, 16(1):3–20, 2003.

[76] Bin Wang, Yongsheng Zhang, and MM Lu. Definition of south china sea monsoon onset and commencement of the east asia summer monsoon. *Journal of Climate*, 17(4):699–710, 2004.

[77] Yongsheng Zhang, Tim Li, Bin Wang, and Guoxiong Wu. Onset of the summer monsoon over the indochina peninsula: Climatology and interannual variations. *Journal of Climate*, 15(22):3206–3221, 2002.

[78] Wen Zhou and Johnny CL Chan. Enso and the south china sea summer monsoon onset. *International Journal of Climatology*, 27(2):157–167, 2007.

[79] Yihui Ding, Zunya Wang, and Ying Sun. Inter-decadal variation of the summer precipitation in east china and its association with decreasing asian summer monsoon. part i: Observed evidences. *International Journal of Climatology*, 28(9):1139–1161, 2008.

[80] Chia Chou, Li-Fan Huang, Jien-Yi Tu, Lishan Tseng, and Yu-Chieh Hsueh. El niño impacts on precipitation in the western north pacific–east asian sector. *Journal of Climate*, 22(8):2039–2057, 2009.

[81] Yu Kosaka, Shang-Ping Xie, Ngar-Cheung Lau, and Gabriel A Vecchi. Origin of seasonal predictability for summer climate over the northwestern pacific. *Proceedings of the National Academy of Sciences*, 110(19):7574–7579, 2013.

[82] Dargan MW Frierson. The dynamics of idealized convection schemes and their effect on the zonally averaged tropical circulation. *Journal of the atmospheric sciences*, 64(6):1959–1976, 2007.

[83] Edmund KM Chang, Sukyoung Lee, and Kyle L Swanson. Storm track dynamics. *Journal of climate*, 15(16):2163–2183, 2002.

[84] Yohai Kaspi and Tapio Schneider. Downstream self-destruction of storm tracks. *Journal of the Atmospheric Sciences*, 68(10):2459–2464, 2011.

[85] RT Pierrehumbert. Local and global baroclinic instability of zonally varying flow. *Journal of the atmospheric sciences*, 41(14):2141–2162, 1984.

[86] Chia Chou and J David Neelin. Mechanisms limiting the northward extent of the northern summer monsoons over north america, asia, and africa. *Journal of climate*, 16(3):406–425, 2003.

[87] José Pinto Peixoto and Abraham H Oort. Physics of climate. 1992.

[88] Jacob Scheff, Richard Seager, Haibo Liu, and Sloan Coats. Are glacials dry? consequences for paleoclimatology and for greenhouse warming. *Journal of Climate*, 30(17):6593–6609, 2017.

[89] Tsing-Chang Chen. Characteristics of summer stationary waves in the northern hemisphere. *Journal of Climate*, 23(17):4489–4507, 2010.

[90] William J Randel and Isaac M Held. Phase speed spectra of transient eddy fluxes and critical layer absorption. *Journal of the atmospheric sciences*, 48(5):688–697, 1991.

[91] Brian J Hoskins and David J Karoly. The steady linear response of a spherical atmosphere to thermal and orographic forcing. *Journal of the Atmospheric Sciences*, 38(6):1179–1196, 1981.